All-Natural Aggregation-Induced Emission-Active Glycyrrhizic Acid Hydrogels for Drug-Resistant Bacteria-Infected Wound Healing

Qing Li,[1,2] Yang Liu,[3] Shiqi Zhang,[1] Xinke Yu,[1] Sili Liu,[1] Zhili Wan,[1,4,] Yang Yuan,[*,5] Paul Van der Meeren,[2] Xiaoquan Yang[1]*

1 Laboratory of Food Proteins and Colloids, School of Food Science and Engineering, Guangdong Province Key Laboratory for Green Processing of Natural Products and Product Safety, South China University of Technology, Guangzhou 510640, China

2 Department of Green Chemistry and Technology, Faculty of Bioscience Engineering, Ghent University, Ghent, 9000, Belgium

3 College of Polymer Science and Engineering, State Key Laboratory of Polymer Materials Engineering, Sichuan University, Chengdu 610065, China

4 Overseas Expertise Introduction Center for Discipline Innovation of Food Nutrition and Human Health (111 Center), Guangzhou 510640, China

5 School of Chemistry and Chemical Engineering, Guangzhou University, Guangzhou, 510006, PR China

AUTHOR INFORMATION

Zhili Wan (*corresponding author)

E-mail: zhiliwan@scut.edu.cn

Fax: (086) 20-87114263

Abstract: Aggregation-induced emission-active (AIE-active) hydrogels with a unique integration of both luminescence behavior and gel properties have attracted increasing attention due to their advanced functionalities and applications. However, the development of biocompatible AIE-active hydrogels with superior luminescence performances and sufficient mechanical strength remains a big challenge in the biomedical field, and particularly, bioactive AIE hydrogels from naturally occurring small molecules are highly desirable for use as ideal dressings in clinical practice of infected wound healing, in terms of their strong intrinsic biological activities, good biocompatibility, as well as facile and environmentally friendly processes. Here, for the first time, we report an all-natural robust AIE-active hydrogel consisting of two natural Chinese herbal molecules, i.e. glycyrrhizic acid (GA) and berberine (BR), which can be developed as green dressings for accelerating methicillin-resistant *Staphylococcus aureus* (MRSA)-infected wound healing. This GN-BR hydrogel is constructed from the self-assembly of supramolecular GA nanofibrils (GN) as well as their interactions with BR molecules, leading to the formation of an aggregated fibrillar network embedded with the GN-BR particles, which endow the hydrogels with a strong fluorescence emission, excellent mechanical strength and structural recovery capacity, and interesting stimuli-responsive fluorescence features. More importantly, benefiting from the intrinsic immunoregulatory effects of GA and BR and the unique AIE properties of GN-BR assembles, the hydrogels exhibit high anti-inflammation and antibacterial abilities, especially effective photodynamic antibacterial capacity through generating reactive oxygen species under visible light. *In vivo* studies show that the AIE-active GN-BR hydrogels can promote MRSA-infected skin wound healing by reducing bacterial infection, inducing macrophage phenotype transformation from M1 to M2, downregulating inflammatory response, facilitating collagen deposition, and enhancing angiogenesis. This all-natural GN-BR herb hydrogel is an ideal and versatile hydrogel dressing exhibiting inherent bioactivities and remarkable AIE properties and has great potential in treating wounds infected with drug-resistant bacteria.

Keywords: AIE-active hydrogels; glycyrrhizic acid; berberine; photodynamic therapy; wound healing

1. Introduction

Fluorescent hydrogels are new fascinating soft materials with interior gel network structures and the additional property of being light-emitting, which shows increasingly important roles in applications ranging from fluorescence sensors and optical devices to fluorescent inks and bioimaging.[1-6] The fluorescence properties of these hydrogels are generally derived from the incorporation of diverse fluorophore entities including quantum dots, carbon dots, and dyes into the gel matrix either through physical mixing or diffusion into the gel network.[5-7] However, most conventional fluorophores used in gel construction often suffer from an aggregation-caused quenching (ACQ) effect in their aggregated state, leading to diminished light-emitting properties which impedes the large-scale production and practical applications of fluorescent hydrogels.[4] Fortunately, the emergence of the aggregation-induced emission (AIE) concept where molecules are non-emissive in their monomeric state while showing bright fluorescence in an aggregated state, opens new strategies for creating fluorescent hydrogels with an enhanced photoluminescence ability, i.e., AIE-active hydrogels,[4,8-10] which makes them more suitable for advanced biomedical applications such as tissue engineering, drug delivery, wound healing, and bioinspired actuators.[1-4] AIE-active hydrogels with reactive oxygen species (ROS) production ability or high photo-thermal transition efficiency after a short period of light exposure show stable and broad-spectrum photodynamic or photothermal antibacterial capacities, which endow them with great potential as an efficient therapy strategy for promoting bacterial-infected wound healing.[11-15] The fabrication of these AIE-active hydrogels typically involves the introduction of AIE fluorescent molecules within the gel matrix or the co-assembly of AIE fluorophores and gelators through covalent or noncovalent interactions.[5-7,16-18] In this context, the AIE substances are inherently compatible with the semi-solid-state or condensed-state characteristic of the gels, showing an enhanced fluorescence emission when incorporated or interacting with the gel matrix due to the prohibition of energy dissipation through non-radiative decay as a result of the restriction of AIE intramolecular motions by the aggregated gel networks.

Moreover, the properties of the gel network can also provide the possibility for regulating the luminescence behavior of AIE substances.[7,18-21] However, up to now, a majority of AIE-active hydrogels are created by using organic solvent-soluble semisynthetic or synthetic AIE substances, which bring a series of problems including high cost, sophisticated synthesis and purification procedures, low biocompatibility and even potential toxicity, thus strongly limiting their applications in food, biomedical and health sciences.[22] Therefore, it is highly desirable to develop the AIE-active hydrogels with high biocompatibility and superior luminescence performance to overcome these limitations and broaden future safe applications.

Bioactive hydrogels formed by naturally occurring low molecular weight herbal compounds constitute a special class of soft materials and are currently garnering significant attention due to their excellent biocompatibility, versatile intrinsic biological activities, as well as facile and environment-friendly processes. These hydrogels are generally obtained through the supramolecular self-assembly of herbal small molecules via non-covalent interactions, which display many encouraging properties including tunable structure and functionality, viscoelastic mechanical performance, and stimuli responsiveness. Glycyrrhizic acid (GA), a natural herb saponin derived from the root of the licorice plant, exhibits a wide range of biological activities including anti-inflammatory, hepatoprotective, anticancer, and antiviral activities. The unique amphiphilic structure of GA, comprising a hydrophobic triterpenoid aglycon moiety (18β-glycyrrhetinic acid) and a hydrophilic di-glucuronic unit, gives rise to supramolecular self-assembly in aqueous solutions, which first forms long and semiflexible GA nanofibrils (GN) with a righthanded twist, 2.5 nm thickness, and 9 nm periodicity, and then assembles into hydrogels with a hydrogen-bond fibrillar network at a concentration exceeding 0.3 wt%.[23,24] Moreover, the presence of multiple functional groups, rigid skeletons, and distinctive stacking behaviors within GA molecules endows them with the capacity to generate a range of derivatives and combined with other substances, which can be used as building blocks for synthesizing supramolecular hydrogels and other multiphase colloidal materials.[25-30] Based on the

unique combination of the inherent multi-biological activities and self-assembly properties of GA, we have successfully fabricated versatile GA-based double-network supramolecular hydrogels with encouraging mechanical features, stimuli-responsive behavior, and multifunctional properties, which show promising applications in controlled cargo release and wound healing.[31, 32] As mentioned above, the assembly of AIE fluorescent molecules within the gel matrix or the co-assembly of AIE fluorophores and gelators can be applied to make AIE-active hydrogels with more complex structures and stronger fluorescent features than a single-component system.[33-35] In preliminary experiments, we surprisingly discovered that through the combination of GA with other natural herbal small molecules (e.g., berberine), novel GA hydrogels with unique AIE phenomenon can be prepared. As a natural bioactive isoquinoline alkaloid isolated from Chinese herbal plants, berberine (BR) has been demonstrated to be a natural AIE-active agents, but only exhibits significant AIE characteristics in the organic solvent solution, e.g., 10-80% tetrahydrofuran solution, due to the intramolecular vibration and twisted intramolecular charge transfer.[36-38] Therefore, we speculate that the formation of unique GA-based AIE-active hydrogels is attributed to the co-assembly of these two natural herbal small molecules, GA and BR, in aqueous conditions, which provides the strategy of fabricating biocompatible AIE-active hydrogels and contributes to addressing their application constraints in food, biomedical and health sciences.

Herein, in this work, we successfully design all-natural bioactive AIE-active hydrogels with strong fluorescence emission, excellent mechanical strength and structural recovery capacity, and interesting stimuli-responsive fluorescence features, which can be used for efficient therapy of bacterial-infected wounds. In this unique system, the self-assembly of supramolecular GA nanofibrils (i.e., GN) as well as their interactions with BR molecules induce the formation of an aggregated fibrillar network embedded with the GN-BR particles, which endows the hydrogels with a strong luminescence property under ultraviolet (UV) irradiation. The resulting AIE-active hydrogels exhibit adequate mechanical strength, high fluorescence intensity, and interesting stimuli-responsive

fluorescence features. More importantly, based on the intrinsic biological activity and immunoregulatory effects of GA and BR molecules and the unique AIE properties, the GN-BR hydrogels possess a high synergy photodynamic antibacterial ability toward drug-resistant *Staphylococcus aureus* (MRSA) and a strong anti-inflammatory capacity. These features make them highly suitable as an ideal wound dressing for effectively reducing the bacterial content through photo-active therapy, modulating macrophage polarization (inducing transition from pro-inflammatory macrophages M1 to anti-inflammatory macrophages M2), lowering inflammation levels, as well as accelerating collagen deposition and neovascularization, thus promoting drug-resistant bacterial (i.e., MRSA) infected wound healing. This work, for the first time, reports the fabrication of all-natural biocompatible AIE-active hydrogels based on natural Chinese herbal molecules, i.e., GA and BR, and demonstrates their promising applications in drug-resistant bacteria-infected wound healing due to the inherent bioactivities and remarkable AIE properties.

2. Materials and Methods

2.1. Materials

Glycyrrhizic acid mono ammonium salt (GA, purity > 98%, molecular weight: 839.98 g/mol) was purchased from Acros Organics (USA). Berberine sulfate hydrate (BR, molecular weight: 433.43 g/mol) was obtained from Aladdin Co., Ltd (Shanghai, China). TrypLE Express Enzyme, 1×penicillin-streptomycin-glutamine, donor equine serum, fetal bovine serum, Hank's balanced salt solution without phenol red (HBSS), Dulbecco's phosphate-buffered saline (DPBS), and mouse TNF-α and IL-6 ELISA kit were purchased from Thermo Fisher Scientific. Methyl-thiazolyl diphenyl-tetrazolium bromide (MTT), dimethylsulfoxide (DMSO), Minimum essential medium eagle (MEM), Dulbecco's modified Eagle's medium (DMEM), and lipopolysaccharide (LPS) (L2880) were purchased from Sigma-Aldrich. The Calcein/PI cell cytotoxicity assay kit and the bicinchoninic acid (BCA) protein assay kit were bought from Beyotime Biotechnology (Shanghai,

China). Gram-positive bacteria of *S. aureus* (ATCC 6538) and MRSA (ATCC43300) were used in our experiments. Other chemicals were of analytical grade. All solutions were prepared using Milli-Q water (18.2 MΩ·cm at 25°C).

2.2. Fabrication of GN-BR Hydrogels

The homogenous GA stock solution (2%, w/v, pH 7.0) was prepared by first dispersing GA powder in water and stirring at 80 °C for 5 min, followed by adjusting the pH of the GA stock solution to 7.0 using sodium hydroxide (4 mM). The BR stock solution (2%, w/v) was obtained by dispersing BR powder in water and stirring at 80 °C for 5 min. The GN-BR hydrogels were obtained by adding BR to the GN solution (pH 7.0), and then decreasing their pH to 4.5 using hydrochloric acid (0.5 mM). The final concentration of GN is 1%, and the BR concentration ranges from 0 to 0.25%, which were named GN, GN-$BR_{0.01}$, GN-$BR_{0.025}$, GN-$BR_{0.05}$, GN-$BR_{0.1}$, and GN-$BR_{0.25}$, respectively. Meanwhile, corresponding GN-BR solutions at lower GN and BR concentrations were prepared following the same procedure. These samples were named GN_x-BR_y, where x is the GN concentration and y means the BR concentration.

2.3. AIE Fluorescence Properties of GN-BR Hydrogels

Fluorescence spectra of hydrogels or hydrogel dilutions were measured using a fluorescence spectrophotometer (F-7100, HITACHI, Japan) with an excitation wavelength of 405 nm, and emission spectra were recorded from 450 to 700 nm. The slit width for the emission spectra was set to 2.5 nm. The pure GN hydrogel and BR solution were used as the control. In the temperature-responsive fluorescence measurement, the temperature of the GN-BR hydrogel was adjusted to the corresponding point before measurements. For the pH-dependent fluorescence study, the pH was tuned to the required point during the sample fabrication process. The fluorescence changes were determined by a fluorescence spectrophotometer and simultaneously observed by a fluorescence microscope after addition of an acidifying agent (glucono-delta-lactone, GDL) into the system to slowly reduce the pH. The quantum yield (QY) and time-resolved photoluminescence of the GN-BR

hydrogels were measured on an Edinburgh FLS980 fluorescence spectrometer. The QY of the hydrogels was carried out with an excitation at 405 nm over a luminescence range of 450-700 nm. The fluorescence lifetime of the hydrogels was measured with excitation at 405 nm.

2.4. Molecular Simulation Study

MD simulation was performed by GROMACS 2021 software to reveal the assembly behavior and fluorescence properties of GN-BR hydrogels. The BR and GN molecules were simulated using the CHARMM general force field. Langevin Integrator was applied and the temperature was maintained at 298 K and the simulation box was maintained at 1 bar by isotropic Parrinello-Rahman barostat. The Lennard-Jones interactions were smoothly switched off between 10 and 12 Å by a forced-based switching function. Long-range electrostatic interactions were calculated using the particle-mesh Ewald (PME) method with an error tolerance of 10^{-5}. The configuration of GN and BR molecules was optimized with the approximate normal coordinate rational function optimizer (ANCopt) using the xTB 6.3 program. Subsequentially, 25 optimized GN and BR molecules were added to a TIP3P water simulation box of 8.5 nm×8.5 nm×8.5 nm with the Packmol package. During the equilibration process, we utilized a time step of 1 fs and the simulations were conducted for over 30 ns. For the production run, constant NPT dynamics were employed with a time step of 2 fs, which extended for more than 300 ns.

2.5. In Vitro Antibacterial Assay

The growth curves of bacteria (OD_{600} test) and standard plate counting assays were used to investigate the antibacterial activity of the GN-BR hydrogels. Hydrogels were prepared by the methods mentioned above under aseptic conditions. Gram-positive *S. aureus* and MRSA fluids were prepared by isolating a single colony from an LB plate and suspending it in 10 mL Luria-Bertani (LB) growth medium and incubated at 37 °C for 12 h with shaking at 100 rpm. The bacterial suspensions were diluted with PBS (0.2 M, pH 7.4) to achieve an absorbance of about 0.65 at 600 nm, which were then diluted 100 times by LB medium. The final diluted bacterial suspensions (10 mL) were

198 incubated with 1 g hydrogels or PBS (i.e., control sample) and incubated at 37 °C with gentle
199 shaking. For the plate counting assays, the bacterial suspensions diluted with sterile PBS (OD_{600} =
200 0.65) were added to the surface of the hydrogel (0.2 g) and divided into three groups including Dark,
201 Light 30 min, and Light 60 min groups. The dark group was incubated in darkness at 37 °C for 4 h.
202 For the light groups, the incubator containing bacteria and samples was exposed to white light (20
203 mW/cm^2) for periods of 30 and 60 min, followed by placing them in darkness for extra times. All
204 groups were then diluted for 10^2-10^6 times. Finally, 100 μL of the diluted suspension was spread on
205 the agar culture plate and incubated at 37 °C for 24 h. The bacteria amount in each group was
206 compared to that in the corresponding control sample (PBS treatment), and the survival ratio of
207 bacteria was calculated by the following formula:

208 $$\text{Survival ratio (\%)} = \frac{\text{Cell count of hydrogels}}{\text{Cell count of control survivor}} \times 100\% \quad (1)$$

209 The bacterial live/dead fluorescent staining, surface morphology characterization, ROS level, and
210 leakage of intracellular protein were performed to illustrate the antibacterial mechanism. The related
211 details were described in Supporting Information.

212 **2.6. In Vitro Cell Cytotoxicity Assay**

213 MTT assays and live-dead staining were used to evaluate the cytotoxicity of the GN-BR hydrogels
214 on the mouse fibroblast cells (L929) and the RAW 264.7 macrophage. Two hydrogel extract liquids
215 were obtained by adding 0.1 g hydrogel to modified Eagle's medium (MEM, 5 mL) and Dulbecco's
216 modified Eagle's medium (DMEM) separately incubated in an incubator (37 °C, 5% CO_2) for 24 h,
217 followed by filtration using 0.22 μm filtering membrane. L929 cells were first cultured in MEM
218 media supplemented with 10% donor equine serum and 1% penicillin-streptomycin solution in an
219 atmosphere of 5% CO_2 at 37 °C for 24 h. Before the assay, the cells were seeded in 96-well
220 microtiter plates at a density of 1×10^4 cells/well and incubated at 37 °C and 5% CO_2 for 24 h. Then,
221 the medium was removed and a fresh medium containing different concentrations of hydrogel extract
222 liquid (1, 3, and 10 mg/mL) was added. After incubation for 24 h, the medium was replaced by fresh

MTT solution (0.5 mg/mL) and cultured with 5% CO_2 at 37 °C for 4 h. The absorption of the samples was measured on a microplate reader at 570 nm. Live-dead staining was then performed to assess the cell cytotoxicity after being cultured with hydrogel-diluted liquid (10 mg/mL) for 24 h, where the live cells were stained by calcein-AM with green fluorescence and dead cells were stained by propidium iodide (PI) with red fluorescence. The cell viability of L929 after incubation with gel extract liquids (10 mg/mL) for different times (24, 48, and 72 h) was then investigated by MTT assays and morphological observation. For cytotoxicity assay on RAW 264.7 macrophages, except that the cell density is 5×10^4 cells/well, the others parameters were the same as in the procedure described above. In all cases, five replicate wells were used for each sample.

2.7. Full-Thickness MRSA-Infected Wound Healing Test

The role of GN-BR hydrogels in wound healing was evaluated by an MRSA-infected full-thickness wound model. Ethical approval was granted by the Animal Ethical Committee of South China University of Technology. Kunming mice (male, 5-6 weeks, 20-30 g) were used as the infected surface wound model. After adapting to the environment for 2 weeks, the dorsal hairs of those mice were removed and a 1 cm diameter circular wound was created in their notum, followed by injecting MRSA suspension (40 μL, 5×10^8 CFU/mL) in the wounds and then being kept for 24 h. All MRSA-infected mice (n=48) were randomly divided into four groups (12 mice per group). The MRSA-infected mice without treatment were set as control. The other three groups were treated with 400 μL of various hydrogels, which were named GN, GN-$BR_{0.25}$, and GN-$BR_{0.25}$-Light, respectively. In particular, after addition of the hydrogels, the wounds in the GN-$BR_{0.25}$-Light group were irradiated by visible white light (20 mW/cm^2) for 10 min. All mice were raised in a single cage to prevent each other from scratching the wound and the hydrogels (400 μL) were added to the wound every day. Three mice in each group were sacrificed and the wounds with adjacent normal skin were collected after being treated for 5 days, and the rest were collected on day 11. The wound was recorded by

247 photographing, and the wound area was measured using Image-J software. The wound area ratio was
248 established as follows:

249 (2) $$Wound\ area\ ratio\ (\%) = \frac{the\ wound\ area\ in\ different\ days}{the\ initial\ wound\ area} \times 100\%$$

250 **2.8. In Vivo Antibacterial and Histological Analysis**

251 The mice were sacrificed after post-treatment for 5 and 11 days and the tissues from wounds were
252 collected. Some of the skin tissues in each group were oscillated evenly in 1 mL of sterilized PBS in
253 an ice bath, and the resulting suspensions were serially diluted and incubated on standard agar
254 culture plates to evaluate the in vivo antibacterial ability of the hydrogels. Some of the wound tissues
255 were used for Hematoxylin and eosin (H&E) staining and Masson trichrome staining analysis.
256 Briefly, MRSA-infected wound tissues treated with hydrogels collected on day 5 and 11 were fixed
257 in 4% paraformaldehyde for 24 h, dehydrated, embedded in paraffin, and cut into 4 μm thickness
258 tissue slices. Those slices were then deparaffinized, rehydrated, and stained with H&E (Solarbio,
259 China) and Masson's trichrome stain kit (Solarbio, China). All slices were observed and
260 photographed by an inverted fluorescence microscope (Hamamatsu Nanozoomer S60).

261 **2.9. Immunohistochemical Analysis**

262 The immunohistochemical staining of regenerated in vitro MRSA-infected wound tissues was
263 performed to analyze the extent of wound neovascularization and the inflammatory response. The
264 tissue sections were processed by deparaffinization, antigen-retrieval (citrated buffer, heat-induced),
265 permeabilization (0.3% Triton PBST), and antigen blocking (goat serum, Solarbio, China). For the
266 wound neovascularization observation, the sections obtained on day 11 were incubated with primary
267 antibodies against CD31. DAPI was employed to visualize nuclei. Moreover, immunohistochemical
268 staining of CD86 and CD206 was carried out on day 11 after injury to observe macrophage
269 infiltration and polarization in the wound site. The pro-inflammatory cytokines of interleukin-6 (IL-6,
270 Servicebio), interleukin 1β (TNF-α, Servicebio), and tumor necrosis factor-α (TNF-α, Servicebio)
271 were utilized to study the inflammatory response of wounds on day 5 and 11. The photographs were

captured using Zeiss LSM 880 and the quantification analysis was carried out by Image-J software. At least three images for each group were used for the quantification.

3. Results and Discussion

3.1. Fabrication of GN-BR AIE-Active Hydrogels

The unique integration of strong luminescence behavior and gel network structure endows the AIE-active hydrogels with wide applications in the biomedical field.[4, 39, 40] Particularly, AIE-active hydrogels with high biocompatibility and intrinsic biological activities are highly desirable for safe use as ideal dressings in the clinical practice of infected wound healing. Our preliminary discovery shows that through the unique combination of supramolecular gelator GA with another natural herbal small molecule, BR, we can create novel GA-based hydrogels with interesting AIE characteristics. Recent studies have demonstrated that BR is an AIE-active natural isoquinoline alkaloid isolated from Chinese herbal plants.[36-38, 41, 42] However, it should be noted that pure BR molecules can only exhibit significant AIE properties in the organic solvent solution, e.g., 10-80% tetrahydrofuran solution, due to the intramolecular vibration and twisted intramolecular charge transfer.[34-36] Therefore, we speculate that the formation of unique GA-based AIE-active hydrogels is attributed to the co-assembly behavior of GA and BR in aqueous solutions. Herein, based on the co-assembly of two natural Chinese herbal small molecules, i.e., a supramolecular gelator GA and an AIE-active natural agent BR, we successfully fabricated an all-natural AIE-active hydrogel (i.e., GN-BR hydrogel), which provides a fabrication strategy of biocompatible AIE-active hydrogels and contributes to addressing their application constraints in the food and biomedical fields. The obtained results show that the self-assembly of supramolecular GA nanofibrils (GN) and their interactions with BR molecules (mainly electrostatic interaction) induce the attachment of BR in the GN surfaces and then promote the aggregation of the GN network as well as the formation of GN-BR particles, which thus lead to the formation of hydrogels with an aggregated fibrillar network embedded with

297 the GN-BR particles. This unique network structure endows the hydrogels with high mechanical
298 strength, superior emission properties, and interesting stimuli-responsive fluorescence features
299 (Scheme 1A). The internal biological activities and immunoregulatory effects of GA and BR as well
300 as the AIE properties provide these hydrogels with excellent anti-inflammatory and antibacterial
301 abilities, especially the effective photodynamic antibacterial capacity through the generation of
302 reactive oxygen species under visible light, thus showing a promoting application in bacterial-
303 infected wound healing (Scheme 1B).
304 As can be seen in Figures 1A and S2A (Supporting Information), pure GN hydrogel (1%) with
305 fibrillar network shows a homogeneous transparent appearance. Upon introduction of BR (0-0.25%)
306 into GN solution at a pH of 7.0 followed by slowly tuning to 4.5, the formed GN-BR hydrogels were
307 changed to a yellow turbid appearance with a more solid state. Surprisingly, the GN-BR hydrogel
308 emits green fluorescence under ultraviolet irradiation and its fluorescence intensity is largely higher
309 than those of pure GN hydrogel and BR aqueous solution (Figures 1A and 2A), which suggests the
310 successful fabrication of GN-BR AIE-active hydrogels with highly fluorescent properties, due to the
311 co-assembly and interactions between GN and BR in water. The resulting hydrogels display a
312 significant three-dimensional (3D) porous network with a more compact structure combined with a
313 lower pore size and an increased pore wall thickness (Figure 1G), as compared to the incompact
314 fibrillar network of pure GN hydrogel (Figure 1F). From the CLSM results, we can observe that the
315 aggregated fibrillar network embedded with the GN-BR particles within the gel matrix exhibits a
316 significant green fluorescence upon excitation at 405 nm (Figures 1B, C, and S3, Supporting
317 Information), further confirming the excellent AIE fluorescence properties. The ESEM results
318 (Figure S2B, Supporting Information) show that these GN-BR particles within the matrix are tightly
319 attached to the aggregated fibrillar network, forming a compact and ordered fibrous network, which
320 can be clearly observed in the hydrogels with a higher BR concentration (especially in GN-$BR_{0.1}$ and
321 GN-$BR_{0.25}$ hydrogels). These microstructural observations together indicate that the co-assembly and

interactions between GN and BR induce the formation of the aggregated fibrillar network embedded with GN-BR particles, which endows the hydrogels with strong mechanical properties and superior AIE fluorescence performances.

We then investigate the co-assembly behavior of GN and BR by adding a low BR concentration (0-0.05%) to the GN solution (0.1%, below the gelation concentration of GN). A more turbid yellow appearance (Figure S1A, Supporting Information) and the aggregated fibrillar network embedded with the GN-BR particles (around 110 nm) could be observed (Figure S1B, Supporting Information), which is attributed to the fact that BR can be efficiently attached to the surfaces of GN through electrostatic interaction (Figure S4E, Supporting Information), further inducing the aggregation of the GN network as well as the formation of GN-BR nanoparticles. We further fabricated samples with a relatively higher concentration of GN (0.2%, slightly lower than the gelation point) and the corresponding BR solutions (0-0.1%). With the increase of the BR concentration, samples with three different states were obtained, including a relatively transparent solution ($GN_{0.2}$ and $GN_{0.2}$-$BR_{0.02}$), yellow gel ($GN_{0.2}$-$BR_{0.05}$), and the solution with a more turbid yellow appearance ($GN_{0.2}$-$BR_{0.1}$) (Figures S1C, Supporting Information). It is worth noting that compared to the pure $GN_{0.2}$ solution, the $GN_{0.2}$-$BR_{0.05}$ shows the particle-attached fibrillar network structure (Figure S1D, Supporting Information). This is due to the formation of GN-BR assembles via electrostatic binding (Figure S5E, Supporting Information), which further increases the interfibrillar aggregation degree and thus induces the formation of hydrogels with a more aggregated fibrillar network. In contrast, when the BR concentration further increases to 0.1%, the $GN_{0.2}$-$BR_{0.1}$ becomes fluid, showing the formation of large particles without observable fibrils (Figure S1D). This structural transition can be explained by the fact that at a high BR concentration (i.e., $GN_{0.2}$-$BR_{0.1}$), most of GN tend to form particles with BR by strong electrostatic interactions and thus there is no sufficient amount of fibrils for the assembly of fibrillar networks. Taken together, the above results demonstrate that all-natural AIE-

active hydrogels with an aggregated fibrillar network embedded with the GN-BR particles can be successfully fabricated by the co-assembly of GN with BR and their mutual interactions.

3.2. Rheological Characterization of GN-BR AIE-Active Hydrogels

The structural viscoelastic properties of GN-BR AIE hydrogels were then determined by using the dynamic oscillatory shear test including linear small amplitude oscillatory shear rheology (SAOS) and nonlinear large amplitude oscillatory shear rheology (LAOS) measurements. Firstly, the strain sweep results of GN-BR hydrogels with 1% GN and different BR concentrations (0-0.25%) are shown in Figure S4A (Supporting information). In all cases, the elastic modulus (G′) of the hydrogel is always significantly higher than the viscous modulus (G″) in their individual linear viscoelastic regions (LVR), indicating the mostly elastic solid-like behavior of these hydrogels. Moreover, it can be clearly seen that the increase of BR concentration significantly increases the values of G′ and G″, indicating the contribution of the GN-BR co-assembly to the gel strength. It is known that the differences in linear and even nonlinear rheological properties between materials can be well reviewed by a yield stress-strain texture map, which can be achieved by analyzing the values of shear stress and strain at the end of the LVR regime (the limit of LVR response using 90% criterion).[43, 44] Generally, soft and non-shaped “mushy” materials (e.g., grits and similar food materials) possess a low yield stress and strain value, and the ones with a “rubbery” texture, such as gelatin, often show low rheological yield stress and high yield strain values. Moreover, samples with high strain and stress values indicate a “tough” texture that is not easily broken (e.g., fruit leather and dried fruits), and ones with a high yield stress and low yield strain like many baked or confectionery food products always represent those “brittle” materials with an easily broken structure.[44] Figure 1J shows the yield strain-stress texture map of GN-BR hydrogels. As can be seen, compared to the GN hydrogel, GN-BR hydrogels, especially those with a higher BR concentration (e.g., GN-$BR_{0.25}$), possess a higher yield stress and a lower yield strain, indicating that GN-BR hydrogels show a more brittle texture

property than pure GN hydrogel. This can be further supported by the crossover strain-stress map (Figure S4B, Supporting Information). Moreover, the power-law model equation of G′ against frequency was adopted to assess the frequency dependence of the GN-BR hydrogels (Figure 1I and Table S1, Supporting Information). The higher value of n′ obtained from the power-law model equation means a higher frequency dependence. As seen, the G′ curves of all hydrogels show a slightly positive slope ($0.11 < n' < 0.28$), which suggests that the rheological response of the hydrogels is not largely affected by the applied deformation rate. The phase angle (δ) between material response and imposed deformation is a measure for how elastic or viscous a material is. It is known that the values of δ equal to 0° and 90° represent a perfectly elastic or viscous material, respectively. The damping factor, tan δ (G″/G′), is often used as an indicator to analyze the contribution of the elastic and viscous components to the viscoelastic response of soft materials. Compared to pure GN hydrogel (G″/G′=0.28), all GN-BR hydrogels show a significantly lower damping factor (Table S1, Supporting Information), suggesting the enhanced elasticity of these hydrogels by the co-assembly of GN and BR. These results indicate that the GN-BR hydrogels are highly elastic soft materials, and their viscoelastic properties can be obviously enhanced by the co-assembly and interactions between GN and BR. Further, to understand the micromechanical response of hydrogels from a nonlinear rheological point of view, the normalized Lissajous-Bowditch plots of GN and GN-$BR_{0.1}$ hydrogels were obtained by using a LAOS analysis at different strains (0.5, 5, and 50%) and a fixed frequency (1 Hz) (Figure 1H). The pure GN hydrogel shows a perfectly elliptical shape in the normalized elastic and viscous Lissajous-Bowditch curves at 0.5 and 5% (within the LVR). Upon increasing the strain to 50%, the normalized elastic and viscous Lissajous curve shapes are shifted to a near parallelogram shape and a near S-shape, respectively (Figure 1Ha and c), suggesting an increase of viscous dissipation during intracycle deformation.[26, 43] In contrast, for the GN-BR hydrogels, there are a perfectly elliptical shape in the normalized elastic and viscous Lissajous-Bowditch curves at strain of 0.5%, suggesting that this hydrogel has an elastic-dominated

behavior at this strain within LVR. Importantly, from the elastic and viscous Lissajous curves, the GN-BR hydrogel shows higher distortion from their original shape with increasing strain (Figure 1Hb and d), as compared to those of the GN hydrogel (Figure 1Ha and c). In details, when the applied strain was increased to 5%, a distortion from their original shape can be observed, i.e., the elliptical shape shifted to near parallelogram shape and a near S-shape in the normalized elastic and viscous Lissajous-Bowditch curves, respectively, which is totally different with these curves in GN hydrogel. Moreover, there are more obvious shape distortions of the normalized Lissajous curves of GN-BR hydrogels at the strain of 50%. These results together suggests that the GN-BR hydrogel has a shift from elastic- to viscous-dominated behavior with strong shear thinning at a lower strain deformation (5%) and shows a relatively higher brittleness property, as compared to pure GN hydrogel, in good agreement with the results in Figure 1J and S4B (Supporting Information).

We then measured the steady-state flow properties of CN-BR hydrogels. As shown in Figure S4C (Supporting Information), the viscosity of all hydrogels decreases with increasing shear rates from 0.01 to 100 s^{-1}, indicating their shear-shinning behavior. With increasing BR concentration, the hydrogels show a higher viscosity at the same shear rate, suggesting a higher gel network strength. Further, to study the thixotropic recovery behavior of hydrogels, a three-interval time test was used to monitor the changes of G′ and G″ values of hydrogels as a function of time under an alternate cycle of low strain (0.1%, within the LVR) and high strain (10%, beyond the LVR). As seen in Figure 1K, in all cases, the G′ is always higher than G″ and there is no apparent change for both moduli at a low strain (0.1%). For all hydrogels, once the applied stain is increased from 0.1 to 10%, their G′ and G″ values are decreased sharply, and the G″ exceeds G′, indicating the destruction of the gel network under large deformation (beyond yield strain). It is worth noting that both moduli can return to their initial values in the first interval when the applied strain is changed to 0.1%. These results strongly indicate that the network structure of the GN-BR hydrogels can be well-restored after deformation. Moreover, we also used the creep test to evaluate the structural recovery of the GN-BR

hydrogels. As shown in Figures 1L and S4D (Supporting Information), for all hydrogels, their strain values decline obviously once the constant stress is removed. These hydrogels, especially the GN-$BR_{0.25}$ hydrogel, show a low maximum creep compliance (J_m=0.01 Pa^{-1}) and a high recovery ratio (47.88%), further confirming the excellent structural recovery ability of the GN-BR hydrogels. The above results together indicate that the GN-BR hydrogels show satisfactory viscoelastic properties, as well as an excellent structural recovery ability, which can meet the material requirements for practical applications.

3.3. AIE-Active Properties of GN-BR Hydrogels

The AIE characteristics of GN-BR hydrogels were investigated by studying their photoluminescence behavior upon excitation at 405 nm. As can be seen in Figure 2A, the free GN and BR solutions show a weak emission profile in the spectral range of 450 to 700 nm with a centered peak at about 545.4 nm, suggesting the almost non-emissive property of GN and BR molecules in water. This is attributed to the fact that both GN and BR molecules in aqueous solutions can form a twisted intramolecular charge transfer (TICT) state and then form H-bonds with water molecule, thus efficiently dissipating their excited state energy through fast non-radiative decay pathways. Interestingly, an obvious enhancement of emission intensity could be observed in the GN-$BR_{0.01}$ hydrogel, which is about 127.5 and 260.2 folds higher than those of GN and BR aqueous solution at 545.4 nm, respectively. This improved emission profile of the GN-BR system may be closely related to the strong binding between GN and BR (Figure S4E, Supporting Information). The co-assembly and binding of GN-BR efficiently inhibit the BR molecular motion and then curtail the non-radiative excitation pathways for the excited substance, further making energy release through a radiative transition (i.e., luminescence), which thus provides the hydrogels with high AIE fluorescent properties. Then, we calculated the emission intensity ratio at 545.4 nm between the GN-BR hydrogels and the corresponding BR or GN solution, namely the relative fluorescence intensity to

BR or GN. As shown in Figure 2C, at the same BR concentration (0.01%), the GN-BR hydrogels with a higher GN concentration show an evident higher relative fluorescence intensity, suggesting a stronger AIE property with increasing GN concentration. The same results could be obtained by comparing the relative fluorescence intensity of samples with a constant GN concentration (1%) and a range of BR concentrations (Figure 2C). These results suggest that the AIE characteristics of the GN-BR system are highly related to the interactions between GN and BR, which is largely dependent on the concentrations of GN and BR. In addition, the quantum yield (QY) of the GN-$BR_{0.01}$ hydrogel is 11.64% and its average fluorescence lifetime at 545.4 nm is 13.34 ns (Figure 2B), suggesting a remarkable AIE property of the BR-GN hydrogel system.

Our previous studies have shown that the GN hydrogel is thermoreversible with a gel-sol transition temperature range of 55-60°C.[23, 24, 31] As expected, the GN-BR hydrogels also show the thermo-responsive behavior as evidenced by the temperature sweep, which shows both G′ and G″ decrease sharply as the temperature reaches about 55°C, and the G″ exceeds G′ at a range of temperature (55-80 °C), followed by an increase of both moduli and G′ over G″ again upon decreasing the temperature from 80 to 25 °C (Figures 2E). Based on this gel-sol reversible transition property of the GN-BR hydrogels, we then systematically investigate the fluorescence emission spectra of the GN-BR hydrogels at different temperatures. It is evident that the maximum emission wavelength of the hydrogels displays a blue shift from 545.4 to 527.0 nm and their fluorescence density gradually increase during the cooling process from 80 to 25 °C (Figure S5A and B, Supporting Information). This is further supported by the corresponding appearance of samples under UV light (Figure 2F). The temperature-dependent fluorescence behavior of the GN-BR hydrogels can be related to the noncovalent hydrogen bonding between fibrils. At a high temperature, the fibrillar network gradually becomes loose due to the weakened noncovalent crosslinking, which enhances the molecular flexibility in terms of vibration, rotation, and translation, thus leading to an acceleration of the non-radiative decay processes and the reduction of the fluorescence intensity. The temperature-responsive

AIE behavior of the GN-BR hydrogels is further assessed by a multi-cycle test at temperatures of 25 and 80 °C. As shown in Figure 2D, the high fluorescence at 25 °C and low fluorescence at 80 °C could be repeated five times, which demonstrates a smart fluorescent hydrogel with tunable emission behavior. Furthermore, the fluorescence properties of the GN-BR hydrogels at different pH are displayed in Figure 2G. Compared to the sample at pH 7, the hydrogels with lower pH values show a higher emission density at 545.4 nm, and in particular, a nearly 41.3-fold fluorescence intensity can be found in the sample at pH 4.5, which is attributed to the fact that the stronger interactions (mainly the electrostatic interactions) between GN and BR at a lower pH could more efficiently inhibit the molecular movement of BR and then increase the emission property. Note that this pH-responsive AIE behavior cannot be observed in the BR solution (Figure S5C, Supporting Information). To achieve an in-situ observation of the pH effect on the fluorescence property of the hydrogels, an acidifying agent (i.e., glucono-delta-lactone solution) was added into the system to slowly reduce the pH after incorporation of GA and BR at pH 7.0, followed by the fluorescence determination. As shown in Figures 2H and I, the fluorescence intensity of the sample increases gradually during the pH-decreasing process accompanied by a blue shift of the maximum emission wavelength, and also the fluorescence region is significantly enlarged, indicating enhanced fluorescence properties, in good agreement with the result of Figure 2G. Taken together, these results confirm that the GN-BR hydrogels are novel AIE-active soft materials, and their stimuli-responsive fluorescence property can be well tuned by changing the pH and temperature of the system.

3.4. AIE-Active Mechanism of GN-BR Hydrogels

We here explore and understand the underlying mechanism of the unique AIE fluorescent behavior of GN-BR hydrogels. We first conducted molecular dynamics (MD) simulations to investigate the assembly behavior of BR and GN. The simulations lasted 300 ns, during which the randomly distributed BR and GN assemble and the resulting snapshot is depicted in Figure 3A. We computed

the radial distribution functions (RDF) for GN-BR, GN-GN, and BR-BR from the simulations, and the corresponding plots are shown in Figure 3C. The positions of the first valleys in the RDF are approximately 0.65, 0.9, and 1.5 nm for BR-BR, GN-BR, and GN-GN, respectively. This indicates that GN molecules have a larger volume compared to BR. Furthermore, we defined two molecules to be in the same cluster if the distance between their centers of mass is shorter than the position of the first valley in the RDF. We calculated the number of clusters, which is illustrated in Figure 3E. Our findings reveal that GN-GN and GN-BR form a stable aggregate, whereas BR-BR forms approximately 5-10 clusters after around 25 ns. This observation is consistent with Figure 3A, which shows BR interspersed in the GN aggregate with gaps formed between them. Throughout the entire simulation, the high contact number values of the three molecule pairs indicate a stable aggregate of GN and BR. The formation of hydrogen bonds between GN-GN and GN-BR molecules (Figure 3B) contributes to the stability of the aggregate.

To gain a better understanding of the mechanism of luminescence resulting from the assembly behavior of BR and GN, we employed Time-Dependent Density Functional Theory (TD-DFT) at the B3LYP/6-311+G (2d, p) level, which can provide insights into the photoluminescence characteristics of BR and GN and contribute a theoretical foundation for their luminescent properties.[45-49] The initial models of BR, GN, and GN-BR systems are extracted from all-atom molecular dynamic simulation in Figures 3A-E. The BR and GN-BR systems used HSO_4^- for charge balance. To quantify the luminescence intensity of the three systems, we computed the highest occupied orbit (HOMO) and the lowest unoccupied orbit (LUMO) energy gap. As shown in Figure 3Fa, the energy gap of BR, GN, and GN-BR were 3.15, 4.58, and 2.81 eV, respectively. Due to limited activity, the probability of non-radiative transitions through motion decreases, while the probability of energy release through a radiative transition, such as luminescence, increases. This decrease in the HOMO-LUMO energy gap leads to aggregation-induced luminescence. A smaller energy gap indicates easier excitation of the molecule. Among the three systems studied, the GN-BR system exhibits the lowest energy gap

and is therefore the most easily excited, emitting the strongest luminescence. This observation agrees with the results in Figure 2. Interactions between the ring structures of BR and GN result in the formation of intermolecular electron clouds, leading to rigid molecular conformation and spatial conjugation, ultimately enhancing emission. Figure 3Fa clearly demonstrates the spatial conjugation effect between the carbon rings of BR and GN, and the interaction between the carbon ring atoms induces changes in the distribution of π electrons (or p electrons) within the system. Furthermore, we analyzed the electrostatic potential diagrams of each system, as depicted in Figure 3Fb. The spatial interaction (TSI) between the ring structures of the GN-BR system results in a modification of the charge distribution on each atom. Upon comparing the electrostatic potential graph, we can observe that the transition from positive to negative charge on each atom corresponds to a change from blue to red, signifying the overlapping of electric clouds. This overlap extends the electric connection and decentralization range, ultimately reducing the HOMO-LUMO energy gap.

The mechanism of the formation of GN-BR hydrogels was also studied with a series of spectroscopy techniques including UV-vis, FTIR, and 1 H-NMR. As seen from the UV-vis spectra (Figure 3G), the GN-BR system (254, 344, and 420 nm) possesses the typical characteristic absorption peaks of both GN (257 nm) and BR (345 and 421 nm) with a slight shift, indicating the successful construction of GN-BR assembles. The FTIR spectroscopy shows that GN possesses typical -OH stretching vibration at 3423 cm^{-1}, C=O stretching at 1727 cm^{-1}, COO^- group stretching vibration at 1593 and 1419 cm^{-1}, CH_2 antisymmetric stretching at 2947 cm^{-1}, and C-H symmetric stretching of CH_3 groups at 2873 cm^{-1}, respectively. Particularly, after binding with BR, the stretching vibrations of the -OH and COO^- are shifted to lower wavenumbers (3412 and 1722 cm^{-1}) (Figure 3H), and the characteristic peak to the quaternary iminium ion ($C=N^+$) at 1636 cm^{-1} (seen in pure BR) disappears, which may be attributed to the hydrogen bonds between GN-GN and GN-BR, as well as the electrostatic interaction between the carboxyl group and quaternary ammonium ion. In addition, as revealed in the ^1H NMR spectra (Figure 3K), the GN-BR assembles have the H signals of GN and

BR, and the chemical shifts of the H signal in GN move from 2.54, 2.15, 1.79, 1.42, 1.12, and 0.82 ppm to 2.48, 2.09, 1.75, 1.36, 1.03, and 0.78 ppm, respectively, after the assembly with BR. It also can be observed that the GN-BR hydrogel has H signals at larger chemical shifts at 9.67, 8.53, 7.96, 7.49, 6.99, 5.16, and 3.35 ppm, as compared to those of pure BR at 9.53, 8.10, 7.88, 7.69, 7.14, 6.03, and 3.12 ppm. These results suggest that the environment of the proton in the glucuronic acid of GN and the unsaturated cycloalkanes in BR is affected by the intermolecular hydrogen bonds and the electrostatic interaction between GN and BR, which is in good agreement with the results of FTIR (Figure 3H). Moreover, the thermodynamic characteristics of the interaction between GN and BR were further studied by ITC. Figure 3I shows the heat flows obtained from BR (1%) titrated water (blank group) and BR (1%) titrated GN (0.05%) (experimental group), and as observed, both titration curves are upward, suggesting an exothermic reaction. The thermodynamic parameters including ΔG, ΔH, and ΔS of the interactions are shown in Figure 3J. The negative Gibbs energy change ($\Delta G < 0$) suggests that the interaction between GN with BR is a spontaneous process. Moreover, it is noted that the binding of GN with BR is exothermic ($\Delta H < 0$) and accompanied by entropy production ($\Delta S > 0$), suggesting an enthalpy-driven reaction mainly by electrostatic interaction.[50-52] These results indicate that through the electrostatic interaction, hydrogen bonding, and π-π stacking between molecules (GA-GA, GA-BR, and BR-BR), the BR can attach to the surface of GN and induce the formation of aggregated fibrillar network and GN-BR particles, which thus efficiently limit the intramolecular vibration and twisted intramolecular charge transfer of BR, reduce the HOMO-LUMO energy gap, and finally release energy through a radiative transition (i.e., luminescence).

3.5. In Vitro Antibacterial Properties of GN-BR AIE-Active Hydrogels

Based on the inherent biological activities of GN and BR herbal molecules and the remarkable AIE property, the GN-BR hydrogels are expected to be ideal biomaterials to fight against bacteria by

classical and photodynamic antibacterial activities. Thereby, we evaluated the antibacterial activity in darkness and the photodynamic antibacterial capacity of the GN-BR hydrogels against Gram-positive *S. aureus* and MRSA. To eliminate the effect of white light, the survival of bacteria is calculated by comparing the bacterial count with the corresponding light control group. It can be observed from the bacterial growth curves (Figure S6A, Supporting Information) that compared to the control (without hydrogel treatment) and pure GN hydrogel, the GN-BR hydrogels (especially GN-$BR_{0.25}$) show lower OD_{600} values at the same culture time, suggesting the higher antibacterial ability against *S. aureus*. Moreover, the plate photographs of cultured bacteria (*S. aureus*) after incubation with GN-BR hydrogels at a low GN (1%) and different BR concentrations (0-0.25%) for 4 h show that the antibacterial ability of the GN-BR hydrogels (especially GN-$BR_{0.25}$) is significantly higher than that of the pure GN hydrogel (Figure 4B), and the survival of *S.aureus* decreased from 83.6% (for the GN hydrogel) to 24.0% (for the GN-$BR_{0.25}$) after treated by these hydrogels (Figure 4A). The enhanced antibacterial ability observed under darkness can be attributed to the effect of BR released from the hydrogels, in which about 40.1 and 62.4% of BR are released after 4 h in PBS at pH conditions of 4.5 and 7, respectively (Figure S6B, Supporting Information). Moreover, the GN-BR hydrogels treated with visible light show a lower bacterial (*S. aureus*) count as compared to the corresponding hydrogel group without light and the GN hydrogel group with light. Especially, for the GN-$BR_{0.05}$ hydrogel group, about 83.9 and 100% of *S. aureus* are killed after irradiation with white light for 30 and 60 min, respectively, which are much higher than in darkness (around 50%). The role of hydrogels against MRSA is seen in Figures 4G and H. As seen from the live-dead staining images, compared to the samples in darkness (dark groups), more red regions showing stained dead bacteria appear in the light groups after irradiation treatment (Figure 4E), indicating the high photodynamic antibacterial ability. The enhanced antibacterial activity of GN-BR hydrogels upon irradiation with white light may be attributed to the production of ROS, which was then determined by using 2′, 7′-dichlorodihydrofluorescein diacetates (DCFH-DA) as an indicator. As

depicted in Figure 4C, compared with the PBS and the GN-BR hydrogel group without light treatment, the emission fluorescence intensity of DCFH-DA in the hydrogel group with light treatment for 30 min is obviously increased, which cannot be observed in the PBS groups with and without light. These results demonstrate that the GN-BR AIE-active hydrogels have an efficient ROS production capability, which is probably related to the energy or electron transfer reactions of BR upon light irradiation.[38, 41]

To further investigate the antibacterial mechanism, we then observed the morphological changes of bacteria by FE-SEM and determined the leakage degree of intracellular protein. As shown in Figures 4D and F, under darkness, the bacteria in the untreated group (control) maintain a smooth surface and intact membranes as well as a normal morphology even when exposed to white light. However, after being cultured with the GN-BR hydrogels (especially GN-$BR_{0.25}$), the cell membrane is broken and there are varying degrees of protein losses in the cell content (Figure 4F). After irradiation with white light for 30 min, more evident cell deformation, surface wrinkles, and holes in the bacteria (indicated by red arrows) as well as higher protein leakage in the cell content are observed (Figure 4D and F), which is attributed to the generated ROS thus damaging the cell membrane. These observations are consistent with the abovementioned antibacterial activity results (Figures 4A, B, E, G, and I). Therefore, based on these results, we speculate that these natural antibacterial substances (e.g., BR) can efficiently bind to the surface of bacteria and then damage the cell membrane, and the high ROS production capability of the GN-BR hydrogels further provide them a high photodynamic antibacterial activity.

3.6. In Vitro Biocompatibility and Anti-Inflammatory Effects of GN-BR AIE-Active Hydrogels

The biocompatibility of materials is an indispensable factor for their practical applications in the biomedical field. To demonstrate the compatibility of GN-BR hydrogels, the cell viability assays of these hydrogels against L929 fibroblasts and RAW264.7 macrophages were performed with the

MTT assay and live-dead cell staining. As shown in Figure 5A, a slight increase in the cell viability of L929 fibroblasts is observed after co-culture with different concentrations of hydrogel extract liquids (1, 3, and 10 mg/mL) for 24 h. After longer incubation time (48 and 72 h), there is still a high cell viability (over 70%) for hydrogel extract solutions (Figure 5B), suggesting the good cytocompatibility of the GN-BR hydrogels. Moreover, after treatment with hydrogel extracts, the live-dead staining images of the L929 cells demonstrate that the majority of the L929 cells are alive since most of the cells with the spindle-like morphology show green fluorescence and only a few of them exhibit red fluorescence, which is further supported by the morphology of L929 cells incubated with hydrogels for different times (24, 48, and 72 h) in Figure S7 (Supporting Information). These results together confirm the good cytocompatibility of the GN-BR hydrogels. Next, a hemolysis test was further used to evaluate the blood compatibility of the GN-BR hydrogels (Figure 5F), in which a clear supernatant and a low hemolysis ratio (< 5%) can be found in the hydrogel treated groups. Moreover, the blood cells have a normal morphology after being treated with the hydrogels (Figure S8, Supporting Information). This indicates that the GN-BR hydrogels have a high biosafety without any apparent hemolysis.

The inherent immunoregulatory ability of GN and BR molecules makes that the GN-BR hydrogels have a great potential as ideal biomaterials to reduce excessive inflammation. Here, we estimate the anti-inflammation ability of the GN-BR hydrogels by using the lipopolysaccharide (LPS) stimulation of RAW264.7 macrophages. After co-culture of RAW264.7 cells with hydrogel extract liquids (1, 3, and 10 mg/mL) for 24 h, the MTT result shows a high cell viability above 80% (Figure 5C). More importantly, the live-dead staining images show that most of cells are alive (green fluorescence) after incubation with the extracted hydrogel liquids (10 mg/mL) for 24 h (Figure 5C). This means that the GN-BR hydrogels also have a high cell biocompatibility for RAW264.7 macrophages, which suggests that they are suitable for the following anti-inflammatory assay. TNF-α and IL-6 were then selected as the representative proinflammation cytokines, which are used to primarily investigate the

effects of hydrogel extracts on the inflammation response. As can be seen in Figures 5G and H, the levels of TNF-α and IL-6 in the LPS group are significantly increased, as compared to that in the control group (without LPS), confirming the successful construction of the LPS-induced cellular inflammation. After the addition of GN and GN-BR hydrogel extract solutions (10 mg/mL) for 24 h, it can be seen that the levels of TNF-α and IL-6 in the cell supernatant are decreased, which is more evident in the hydrogels with higher BR concentrations. This demonstrates that the GN-BR hydrogels can relieve inflammation reaction by inhibiting the pro-inflammatory mediator, and thus are an efficient treatment option for diseases caused by immune overreaction.

3.7. MRSA-Infected Full-Thickness Wound Healing Ability of GN-BR AIE-Active Hydrogels

The above results together demonstrate that the GN-BR hydrogels have sufficient mechanical strength, remarkable AIE properties, good biocompatibility, excellent anti-inflammation effects, and high photodynamic antibacterials ability, which make them highly suitable as ideal hydrogel dressings for promoting wound healing. Therefore, an MRSA-infected full-thickness model was constructed to evaluate the wound healing efficacy in vivo of the GN-BR hydrogels (Figure 6A). Briefly, a circular wound (10 mm) on the back of mice was first infected with 40 μL of MRSA (5×10^8 CFU/mL). These mice were then randomly divided into four groups: the control (without treatment), GN, GN-$BR_{0.25}$, and GN-$BR_{0.25}$ Light groups. 400 μL of hydrogels were injected into the wound site to cover the wound bed for all hydrogel groups. Among them, the GN-$BR_{0.25}$ Light group was treated with the corresponding hydrogel and an additional visible light irradiation (20 mW/cm^2) for 10 min. Figure 6B shows representative sequential pictures of wounds on different time points (day 0, 1, 3, 5, 7, 9, and 11), and the corresponding wound area ratio for each group was calculated and shown in Figure 6C. As expected, the hydrogel-treated groups, especially the GN-BR hydrogels with and without visible light irradiation (i.e., GN-$BR_{0.25}$ and GN-$BR_{0.25}$ Light), possess smaller remaining wound areas compared to the control group (without hydrogel treatment) and pure GN

hydrogel group during the treatment periods. On day 5, the wound area ratio in the control group is about 76.5%, whereas the GN-$BR_{0.25}$ and GN-$BR_{0.25}$ Light groups show wound area ratios of 72.8 and 65.2%, respectively, indicating the efficient therapy effects of the GN-BR hydrogels. It is worth noting that, on day 11, there is a relatively lower residual wound area with a ratio of about 13.7% for the GN-$BR_{0.25}$ Light group as compared to that for the corresponding hydrogel without additional irradiation treatment (about 16.9%), which indicates that the photodynamic effect further promotes wound healing. Then, the antibacterial activity in vivo was further evaluated quantitatively by examining and counting bacterial growth on the skin wounds. From the representative photographs and antibacterial ratio results (Figures 6D and E), we can find that on days 5 and 11, the GN-BR hydrogel-treated groups under darkness exhibit decreased bacterial amounts as compared to the control and pure GN hydrogel groups, which suggests that the GN-BR hydrogels could more efficiently eliminate MRSA in the wounds mainly through the release of bioactive BR (Figure S6B, Supporting Information). Moreover, the number of bacteria in the wound of the light group (GN-$BR_{0.25}$ Light) is significantly lower than those of other three groups (Figures 6D and E), indicating a stronger antibacterial ability under light conditions than in darkness. This suggests that the GN-BR hydrogels, especially the GN-BR hydrogels combined with irradiation, possess a strong efficacy in promoting wound healing.

The H&E and Masson's trichrome staining of wound skins after 5 and 11 days of treatments were then performed to reveal the histopathological structures of skins during the wound healing process and to further analyze the role of the GN-BR hydrogels in wound healing. From the HE stains results (Figure 6G), we can observe that a few of epidermis formed in the control group on day 5, while the hydrogel groups show the dermis layers with higher regularity and connective tissue and partial epithelium layer. Notably, on day 11, the control group has a thick epidermis thickness, suggesting it is still in the stage of tissue remodeling and differentiation. In contrast, a completely thinner epidermal layer (blue arrow), well-organized dermis, and more hair follicles (green arrow) are

observed in the hydrogel groups, which further confirms the positive roles of the GN-BR hydrogels in accelerating wound healing. The length of the wound edge in HE staining images was also calculated and shown in Figure 7D. As can be seen, the GN-BR hydrogels with and without irradiation show shorter wound lengths than the control group. Collagen deposition is one of the significant indicators of the integrity of skin repair during the remodeling phase. The Masson's trichrome staining was used to explore the level of collogen in wound tissues after different hydrogel treatments. As can be seen in Figures 6F, H, and S9 (Supporting Information), more and denser regular collagen deposition showing deeper blue staining are observed in the GN-BR hydrogel groups (especially the GN-$BR_{0.25}$ Light group), as compared to the control and GN hydrogel group after treatment for 5 and 11 days. Moreover, the GN-BR hydrogel group, especially the GN-$BR_{0.25}$ Light group, shows a high collagen fraction (56.0%) while the control group only exhibits a low value (28.1%) on day 11 (Figure 6F), demonstrating that the GN-BR hydrogels effectively promote collagen deposition and contribute to skin regeneration. These results together suggest that the GN-BR hydrogels could promote the formation of the epidermis and facilitate skin regeneration.

Blood vessels play an important role in providing nutrients and oxygen to the cells, thus accelerating wound healing. Platelet endothelial cell adhesion molecule-1 (CD31) is primarily expressed in endothelial cells and is considered a critical indicator of angiogenesis. Thereby, to further illustrate the role of the GN-BR hydrogels in promoting wound skin angiogenesis formation, an immunofluorescence assay was performed to evaluate the expression of CD31 molecules stained in the wounds on day 11. As shown in Figure 7A, there are few CD31 expressed in the control group, and as a contrast, more angiogenesis (the red fluorescence indicated by orange arrows) appear in the GN-BR hydrogel groups (especially the GN-$BR_{0.25}$ Light), meaning the stronger formation ability of angiogenesis. Meanwhile, the amount of angiogenesis in the GN-BR hydrogel groups is higher than those in the control and pure GN hydrogel group (Figure 7E), suggesting that the GN-BR hydrogels

are more effective in promoting the formation of angiogenesis, which may be highly related to the high antibacterial effect and also photodynamic antibacterial ability.

The macrophages are important phagocytes of the innate immune system, which play a crucial role in modulating inflammation and promoting wound healing. Generally, the macrophages show a low switch ability from the M1 to M2 phenotype in the bacterial-infected wounds due to the high bacterial effects, thus accumulating the inflammatory cells, releasing more inflammatory factors, and leading to a prolonged inflammation stage. For efficient bacterial-infected wound healing, it is crucial to promote the shift from the pro-inflammatory M1 macrophage to the anti-inflammatory M2 macrophage and to accelerate the conversion from inflammation to the normal proliferative phase. Therefore, we further analyzed the effects of the GN-BR hydrogels on regulating macrophages polarization and reducing the inflammation level. As shown in Figure 7C, compared to the control group, the level of CD86 (M1 marker) decreases and the CD206 (M2 marker) increases after treatment of hydrogels, especially the GN-BR hydrogels, suggesting the effective transition from M1 to M2 macrophages. This reveals that the GN-based hydrogels have significant anti-inflammatory activity through regulating the polarization of macrophages, which is probably due to the inherent immunoregulation ability of these two natural herbal molecules, i.e., GA and BR. To further clarify the anti-inflammation effect of the hydrogels, the expression of typical pro-inflammatory cytokines including tumor necrosis factor (TNF-α), interleukin 1β (IL-1β), and interleukin 6 (IL-6) on the wounds after treatments of 5 and 11 days was analyzed using immunohistochemistry staining. As shown in Figures 7B and F-H, and S10 (Supporting Information), there is an obviously lower inflammatory response (less pro-inflammatory cells) in the GN-BR hydrogel groups, as compared to that in the control group, indicating that the GN-BR hydrogels effectively downregulate the pro-inflammation level. Taken together, these results demonstrate that the GN-BR hydrogels possess an excellent skin regeneration ability by promoting epidermis generation, vessel formation, and collagen deposition, as well as inhibiting bacteria growth, modulating macrophage polarization from M1 to

M2 phenotypes, and mitigating inflammatory response through downregulating the pro-inflammation factor. Moreover, benefiting from their high AIE fluorescence property and ROS generation ability, the GN-BR AIE-active hydrogels could be used as efficient photodynamic antibacterial biomaterials for combatting and reversing bacterial infections in wounds, thus accelerating the bacterial-infected wound repair and healing.

4. Conclusions

In summary, we have successfully created a novel all-natural robust AIE-active hydrogel consisting of two natural Chinese herbal molecules, i.e. GA and BR, which can be used as ideal bioactive hydrogel dressings for accelerating MRSA-infected wound healing. This GN-BR hydrogel is constructed from the self-assembly of supramolecular GN as well as their interactions with BR, leading to the formation of aggregated fibrillar network embedded with the GN-BR particles, which endow the hydrogels with a strong fluorescence emission. This is because the aggregated gel network can efficiently inhibit the BR molecular motion and curtail the non-radiative excitation pathways for the excited molecules, thus causing energy release through a radiative transition. Moreover, compared to pure GN fibrillar hydrogel, the particles-attached aggregated GN-BR fibrillar network provides these AIE-active hydrogels with stronger mechanical properties, a higher structural recovery ability, and interesting stimuli-responsive (i.e., pH and temperature) fluorescence features. Notably, benefiting from the intrinsic biological activities and immunoregulatory roles of the two building block molecules (GA and BR), the GN-BR hydrogels exhibit a high traditional antibacterial ability as well as synergistic photodynamic antibacterial capacity against *S. aureus* and MRSA and also strong anti-inflammatory effects. The *in vivo* results show that the biocompatible GN-BR AIE-active hydrogels could be used as an efficient dressing for accelerating MRSA-infected wound healing by reducing bacterial infection, promoting macrophage polarization from the M1 to M2 phenotype, downregulating inflammatory response, facilitating collagen deposition, and enhancing

neovascularization. To our knowledge, this is the first report describing that all-natural biocompatible AIE-active hydrogels are created based on natural Chinese herbal molecules, which can serve as ideal and versatile bioactive hydrogel dressings for treating wounds infected with drug-resistant bacteria.

Supporting Information

Supplementary experimental methods; Storage modulus (G′) in the linear viscoelastic regime (LVR), power-law exponent (n′), damping factor (G″/G′) values from the frequency curves, and the maximum creep compliance (*J*m) and percentage recovery from the creep curves of the GN-BR hydrogels; Photographs, TEM, and FE-SEM images of GN-BR assembled solutions; Photographs, ESEM images, CLSM images, rheological properties, fluorescence emission spectra, and the BR release ratio of GN-BR AIE hydrogels; OD_{600} growth curves of S. aureus and the microscopy images of L929 cells and blood cells after treatments with GN-BR AIE hydrogels; Masson's trichrome staining images of wound tissues after treatments with GN hydrogel and GN-BR hydrogels with and without white visible light irradiation on day 5; Immunohistochemistry staining images of TNF-α, IL-1β, and IL-6 in wound tissues after treatments with the GN-BR hydrogels with and without white visible light irradiation on day 11 (PDF).

Notes

The authors declare no competing financial interest

Acknowledgments

This work is financially supported by the Outstanding Youth Project of Guangdong Natural Science Foundation (2024B1515020081), the National Natural Science Foundation of China (32172347), and the 111 Project (B17018).

References

(1) Lou, X. Y.; Zhang, G.; Song, N.; Yang, Y. W., Supramolecular Materials Based on AIEgens for Photo-Assisted Therapy. *Biomaterials* **2022**, *286*, 121595.

(2) Xie, H.; Wang, Z.; Wang, R.; Chen, Q.; Yu, A.; Lu, A., Self-Healing, Injectable Hydrogel Dressing for Monitoring and Therapy of Diabetic Wound. *Adv. Funct. Mater.* **2024**, 2401209.

(3) Cao, X.; Gao, A.; Hou, J. T.; Yi, T., Fluorescent Supramolecular Self-Assembly Gels and Their Application as Sensors: A Review. *Coord. Chem. Rev.* **2021**, *434*, 213792.

(4) Li, Z.; Ji, X.; Xie, H.; Tang, B. Z., Aggregation-Induced Emission-Active Gels: Fabrications, Functions, and Applications. *Adv. Mater.* **2021**, *33* (33), e2100021.

(5) Lu, W.; Wei, S.; Shi, H.; Le, X.; Yin, G.; Chen, T., Progress in Aggregation-Induced Emission-Active Fluorescent Polymeric Hydrogels. *Aggregate* **2021**, *2* (3), e37.

(6) Li, Y.; Young, D. J.; Loh, X. J., Fluorescent Gels: A Review of Synthesis, Properties, Applications and Challenges. *Mater. Chem. Front.* **2019**, *3* (8), 1489-1502.

(7) Yuan, J.; Wu, W.; Guo, L.; Hao, J.; Dong, S., Multistimuli-Responsive and Antifreeze Aggregation-Induced Emission-Active Gels Based on CuNCs. *Langmuir* **2022**, *38* (1), 343-351.

(8) Hong, Y.; Lam, J. W.; Tang, B. Z., Aggregation-Induced Emission: Phenomenon, Mechanism and Applications. *Chem. Commun*, **2009**, *29*, 4332-4353.

(9) Li, X.; Li, M.; Yang, M.; Xiao, H.; Wang, L.; Chen, Z.; Liu, S.; Li, J.; Li, S.; James, T. D., "Irregular" Aggregation-Induced Emission Luminogens. *Coord. Chem. Rev.* **2020**, *418*, 213358.

(10) Chen, Y.; Lam, J. W. Y.; Kwok, R. T. K.; Liu, B.; Tang, B. Z., Aggregation-Induced Emission: Fundamental Understanding and Future Developments. *Mater. Horiz.* **2019**, *6* (3), 428-433.

(11) Xu, Y.; Chen, H.; Fang, Y.; Wu, J., Hydrogel Combined with Phototherapy in Wound Healing. *Adv. Healthcare Mater*. **2022**, *11* (16), e2200494.

(12) Zhang, W.; Wang, B.; Xiang, G.; Jiang, T.; Zhao, X., Photodynamic Alginate Zn-MOF Thermosensitive Hydrogel for Accelerated Healing of Infected Wounds. *ACS Appl. Mater. Interfaces*

2023, *15* (19), 22830-22842.

(13) Maleki, A.; He, J.; Bochani, S.; Nosrati, V.; Shahbazi, M. A.; Guo, B., Multifunctional Photoactive Hydrogels for Wound Healing Acceleration. *ACS Nano* **2021**, *15* (12), 18895-18930.

(14) Hu, H.; Zhong, D.; Li, W.; Lin, X.; He, J.; Sun, Y.; Wu, Y.; Shi, M.; Chen, X.; Xu, F.; Zhou, M., Microalgae-Based Bioactive Hydrogel Loaded with Quorum Sensing Inhibitor Promotes Infected Wound Healing. *Nano Today* **2022**, *42*, 101368.

(15) Wang, W.; Wu, F.; Zhang, Q.; Zhou, N.; Zhang, M.; Zheng, T.; Li, Y.; Tang, B. Z., Aggregation-Induced Emission Nanoparticles for Single Near-Infrared Light-Triggered Photodynamic and Photothermal Antibacterial Therapy. *ACS Nano* **2022**, *16* (5), 7961-7970.

(16) Wang, Y.; Zhao, J.; Dong, Z.; Wang, C.; Meng, H.; Li, Y.; Jin, H.; Wang, C., Aggregation-Induced Emission-Active Antibacterial Hydrogel with Self-Indicating Ability for Real-Time Monitoring of Drug Release Process. *Mater. Today Chem.* **2021**, *21*, 100537.

(17) Li, X. F.; Zhou, W.; Liu, Y. C.; Hou, M.; Feng, G. L.; Ji, Y. M.; Zhang, Y.; Xing, G. W., Design and Assembly of AIE-Active Fluorescent Organic Nanoparticles for Anti-Counterfeiting Fluorescent Hydrogels and Inks. *Chem. Commun.* **2022**, *58* (82), 11547-11550.

(18) Yan, X.; Wang, T.; Li, H.; Zhang, L.; Xin, H.; Lu, G., Flexible Aggregation-Induced Emission-Active Hydrogel for On-Site Monitoring of Pesticide Degradation. *ACS Nano* **2022**, *16* (11), 18421-18429.

(19) Cheng, Q.; Hao, A.; Xing, P., Stimulus-Responsive Luminescent Hydrogels: Design and Applications. *Adv. Colloid Interface Sci.* **2020**, *286*, 102301.

(20) Li, B.; Zhang, Y.; Yan, B.; Xiao, D.; Zhou, X.; Dong, J.; Zhou, Q., A Self-Healing Supramolecular Hydrogel with Temperature-Responsive Fluorescence Based on an AIE Luminogen. *RSC Adv.* **2020**, *10* (12), 7118-7124.

(21) Zhang, C.; Li, Y.; Xue, X.; Chu, P.; Liu, C.; Yang, K.; Jiang, Y.; Chen, W. Q.; Zou, G.; Liang, X. J., A Smart pH-Switchable Luminescent Hydrogel. *Chem. Commun.* **2015**, *51* (20), 4168-4171.

(22) Lee, M. M. S.; Yu, E. Y.; Chau, J. H. C.; Lam, J. W. Y.; Kwok, R. T. K.; Wang, D.; Tang, B. Z., Inspiration from Nature: BioAIEgens for Biomedical and Sensing Applications. *Biomaterials* **2022**, *288*, 121712.

(23) Wan, Z.; Sun, Y.; Ma, L.; Guo, J.; Wang, J.; Yin, S.; Yang, X., Thermoresponsive Structured Emulsions Based on the Fibrillar Self-Assembly of Natural Saponin Glycyrrhizic Acid. *Food Funct.* **2017**, *8* (1), 75-85.

(24) Saha, A.; Adamcik, J.; Bolisetty, S.; Handschin, S.; Mezzenga, R., Fibrillar Networks of Glycyrrhizic Acid for Hybrid Nanomaterials with Catalytic Features. *Angew. Chem., Int. Ed. Engl.* **2015**, *54* (18), 5408-5412.

(25) Li, Q.; He, Q.; Xu, M.; Li, J.; Liu, X.; Wan, Z.; Yang, X., Food-Grade Emulsions and Emulsion Gels Prepared by Soy Protein-Pectin Complex Nanoparticles and Glycyrrhizic Acid Nanofibrils. *J. Agric. Food Chem.* **2020**, *68* (4), 1051-1063.

(26) Li, Q.; Xu, M.; Xie, J.; Su, E.; Wan, Z.; Sagis, L. M. C.; Yang, X., Large Amplitude Oscillatory Shear (LAOS) for Nonlinear Rheological Behavior of Heterogeneous Emulsion Gels Made from Natural Supramolecular Gelators. *Food Res. Int.* **2021**, *140*, 110076.

(27) Li, Q.; Xu, M.; Yang, Y.; Guo, J.; Wan, Z.; Yang, X., Tailoring Structure and Properties of Long-Lived Emulsion Foams Stabilized by a Natural Saponin Glycyrrhizic Acid: Role of Oil Phase. *Food Res. Int.* **2021**, *150* (Pt A), 110733.

(28) Li, Q.; Wan, Z.; Yang, X., Glycyrrhizic Acid: Self-Assembly and Applications in Multiphase Food Systems. *Curr. Opin. Food Sci.* **2022**, *43*, 107-113.

(29) Qian, Y.; Zheng, Y.; Jin, J.; Wu, X.; Xu, K.; Dai, M.; Niu, Q.; Zheng, H.; He, X.; Shen, J., Immunoregulation in Diabetic Wound Repair with a Photoenhanced Glycyrrhizic Acid Hydrogel Scaffold. *Adv. Mater.* **2022**, *34* (29), e2200521.

(30) Pi, W.; Wu, L.; Lu, J.; Lin, X.; Huang, X.; Wang, Z.; Yuan, Z.; Qiu, H.; Zhang, J.; Lei, H.; Wang, P., A Metal Ions-Mediated Natural Small Molecules Carrier-Free Injectable Hydrogel Achieving

Laser-Mediated Photo-Fenton-Like Anticancer Therapy by Synergy Apoptosis/Cuproptosis/Anti-Inflammation. *Bioact. Mater* **2023**, *29*, 98-115.

(31) Li, Q.; Zhang, S.; Du, R.; Yang, Y.; Liu, Y.; Wan, Z.; Yang, X., Injectable Self-Healing Adhesive Natural Glycyrrhizic Acid Bioactive Hydrogel for Bacteria-Infected Wound Healing. *ACS Appl. Mater. Interfaces* **2023**, *15* (14), 17562-17576.

(32) Li, Q.; Yu, X.; Zhang, S.; Xu, M.; Yang, Y.; Wan, Z.; Yang, X., All-Natural, Robust, and pH-Responsive Glycyrrhizic Acid-Based Double Network Hydrogels for Controlled Nutrient Release. *ACS Appl. Mater. Interfaces* **2023**, *15* (37), 43633-43647.

(33) Guo, W. J.; Peng, T.; Zhu, W.; Ma, S.; Wang, G.; Li, Y.; Liu, B.; Peng, H. Q., Visualization of Supramolecular Assembly by Aggregation-Induced Emission. *Aggregate* **2022**, *4* (2).

(34) Wang, J.; Qiao, W.; Li, X.; Zhao, H.; Zhang, H.; Dong, A.; Yang, X., A Directed Co-Assembly of Herbal Small Molecules into Carrier-Free Nanodrugs for Enhanced Synergistic Antitumor Efficacy. *J. Mater. Chem. B* **2021**, *9* (4), 1040-1048.

(35) Feng, H. T.; Lam, J. W. Y.; Tang, B. Z., Self-Assembly of AIEgens. *Coord. Chem. Rev.* **2020**, *406*, 213142.

(36) Gu, Y.; Zhao, Z.; Su, H.; Zhang, P.; Liu, J.; Niu, G.; Li, S.; Wang, Z.; Kwok, R. T. K.; Ni, X. L.; Sun, J.; Qin, A.; Lam, J. W. Y.; Tang, B. Z., Exploration of Biocompatible AIEgens from Natural Resources. *Chem. Sci.* **2018**, *9* (31), 6497-6502.

(37) Lee, M. M. S.; Zheng, L.; Yu, B.; Xu, W.; Kwok, R. T. K.; Lam, J. W. Y.; Xu, F.; Wang, D.; Tang, B. Z., A Highly Efficient and AIE-Active Theranostic Agent from Natural Herbs. *Mater. Chem. Front.* **2019**, *3* (7), 1454-1461.

(38) Xie, Y. Y.; Zhang, Y. W.; Liu, X. Z.; Ma, X. F.; Qin, X. T.; Jia, S. R.; Zhong, C., Aggregation-Induced Emission-Active Amino Acid/Berberine Hydrogels with Enhanced Photodynamic Antibacterial and Anti-Biofilm Activity. *Chem. Eng. J.* **2021**, *413*, 127542.

(39) Wang, H.; Li, Q.; Alam, P.; Bai, H.; Bhalla, V.; Bryce, M. R.; Cao, M.; Chen, C.; Chen, S.; Chen,

X.; Chen, Y.; Chen, Z.; Dang, D.; Ding, D.; Ding, S.; Duo, Y.; Gao, M.; He, W.; He, X.; Hong, X.; Hong, Y.; Hu, J. J.; Hu, R.; Huang, X.; James, T. D.; Jiang, X.; Konishi, G. I.; Kwok, R. T. K.; Lam, J. W. Y.; Li, C.; Li, H.; Li, K.; Li, N.; Li, W. J.; Li, Y.; Liang, X. J.; Liang, Y.; Liu, B.; Liu, G.; Liu, X.; Lou, X.; Lou, X. Y.; Luo, L.; McGonigal, P. R.; Mao, Z. W.; Niu, G.; Owyong, T. C.; Pucci, A.; Qian, J.; Qin, A.; Qiu, Z.; Rogach, A. L.; Situ, B.; Tanaka, K.; Tang, Y.; Wang, B.; Wang, D.; Wang, J.; Wang, W.; Wang, W. X.; Wang, W. J.; Wang, X.; Wang, Y. F.; Wu, S.; Wu, Y.; Xiong, Y.; Xu, R.; Yan, C.; Yan, S.; Yang, H. B.; Yang, L. L.; Yang, M.; Yang, Y. W.; Yoon, J.; Zang, S. Q.; Zhang, J.; Zhang, P.; Zhang, T.; Zhang, X.; Zhang, X.; Zhao, N.; Zhao, Z.; Zheng, J.; Zheng, L.; Zheng, Z.; Zhu, M. Q.; Zhu, W. H.; Zou, H.; Tang, B. Z., Aggregation-Induced Emission (AIE), Life and Health. *ACS Nano* **2023**, *17* (15), 14347-14405.

(40) Wang, Z.; Nie, J.; Qin, W.; Hu, Q.; Tang, B. Z., Gelation Process Visualized by Aggregation-Induced Emission Fluorogens. *Nat. Commun.* **2016**, *7*, 12033.

(41) Li, F.; Zhe, T.; Ma, K.; Li, R.; Li, M.; Liu, Y.; Cao, Y.; Wang, L., A Naturally Derived Nanocomposite Film with Photodynamic Antibacterial Activity: New Prospect for Sustainable Food Packaging. *ACS Appl. Mater. Interfaces* **2021**, *13* (44), 52998-53008.

(42) Li, T.; Wang, P.; Guo, W.; Huang, X.; Tian, X.; Wu, G.; Xu, B.; Li, F.; Yan, C.; Liang, X. J.; Lei, H., Natural Berberine-Based Chinese Herb Medicine Assembled Nanostructures with Modified Antibacterial Application. *ACS Nano* **2019**, *13* (6), 6770-6781.

(43) Wang, G. S.; Li, Q.; Feng, G. X.; Han, C. W.; Guo, J.; Wang, J. M.; Wan, Z. L.; Yang, X. Q., Linear and Nonlinear Rheological Characterization of Capillary Protein Oleogels as Potential Fat Replacers: Comparison with High Internal-Phase Emulsions. *Food Hydrocolloids* **2024**, *151*, 109824.

(44) Schreuders, F. K. G.; Schlangen, M.; Bodnár, I.; Erni, P.; Boom, R. M.; van der Goot, A. J., Structure Formation and Non-Linear Rheology of Blends of Plant Proteins with Pectin and Cellulose. *Food Hydrocolloids* **2022**, *124*, 107327.

(45) Guo, L.; Yan, L.; He, Y.; Feng, W.; Zhao, Y.; Tang, B. Z.; Yan, H., Hyperbranched Polyborate: A

Non-conjugated Fluorescent Polymer with Unanticipated High Quantum Yield and Multicolor Emission. *Angew. Chem., Int. Ed. Engl.* **2022**, *61* (29), e202204383.

(46) Wang, L.; Li, W.; Li, F.; Zeng, M., Mechanism of Enhancing Chlorophyll Photostability through Light-Induced Chlorophyll/Phycocyanin Aggregation. *J. Agric. Food Chem.* **2023,** *71* (48), 19010-19019.

(47) Wang, Z.; Zou, X.; Xie, Y.; Zhang, H.; Hu, L.; Chan, C. C. S.; Zhang, R.; Guo, J.; Kwok, R. T. K.; Lam, J. W. Y.; Williams, I. D.; Zeng, Z.; Wong, K. S.; Sherrill, C. D.; Ye, R.; Tang, B. Z., A Nonconjugated Radical Polymer with Stable Red Luminescence in the Solid State. *Mater. Horiz.* **2022**, *9* (10), 2564-2571.

(48) Yuan, L.; Yan, H.; Bai, L.; Bai, T.; Zhao, Y.; Wang, L.; Feng, Y., Unprecedented Multicolor Photoluminescence from Hyperbranched Poly(amino ester)s. *Macromol. Rapid Commun.* **2019**, *40* (17), e1800658.

(49) Zhang, Z.; Zhang, H.; Kang, M.; Li, N.; Wang, D.; Tang, B. Z., Oxygen and Sulfur-Based Pure N-Electron Dendrimeric Systems: Generation-Dependent Clusteroluminescence towards Multicolor Cell Imaging and Molecular Ruler. *Sci.China: Chem.* **2021**, *64* (11), 1990-1998.

(50) Feng, G.; Han, K.; Li, Y.; Yang, Q.; Feng, W.; Wang, J.; Yang, X., Undigestible Gliadin Peptide Nanoparticles Penetrate Mucus and Reduce Mucus Production Driven by Intestinal Epithelial Cell Damage. *J. Agric. Food. Chem.* **2021**, *69* (28), 7979-7989.

(51) Feng, G.; Han, K.; Yang, Q.; Feng, W.; Guo, J.; Wang, J.; Yang, X., Interaction of Pyrogallol-Containing Polyphenols with Mucin Reinforces Intestinal Mucus Barrier Properties. *J. Agric. Food Chem.* **2022**, *70* (30), 9536-9546.

(52) Patel, A. R.; Seijen-ten-Hoorn, J.; Heussen, P. C.; Drost, E.; Hazekamp, J.; Velikov, K. P., Straightforward Preparation of Organic Colloidal Particles by Harnessing Spontaneous Non-Covalent Interactions of Active Molecules from Natural Origin. *J. Colloid Interface Sci.* **2012**, *374* (1), 150-156.

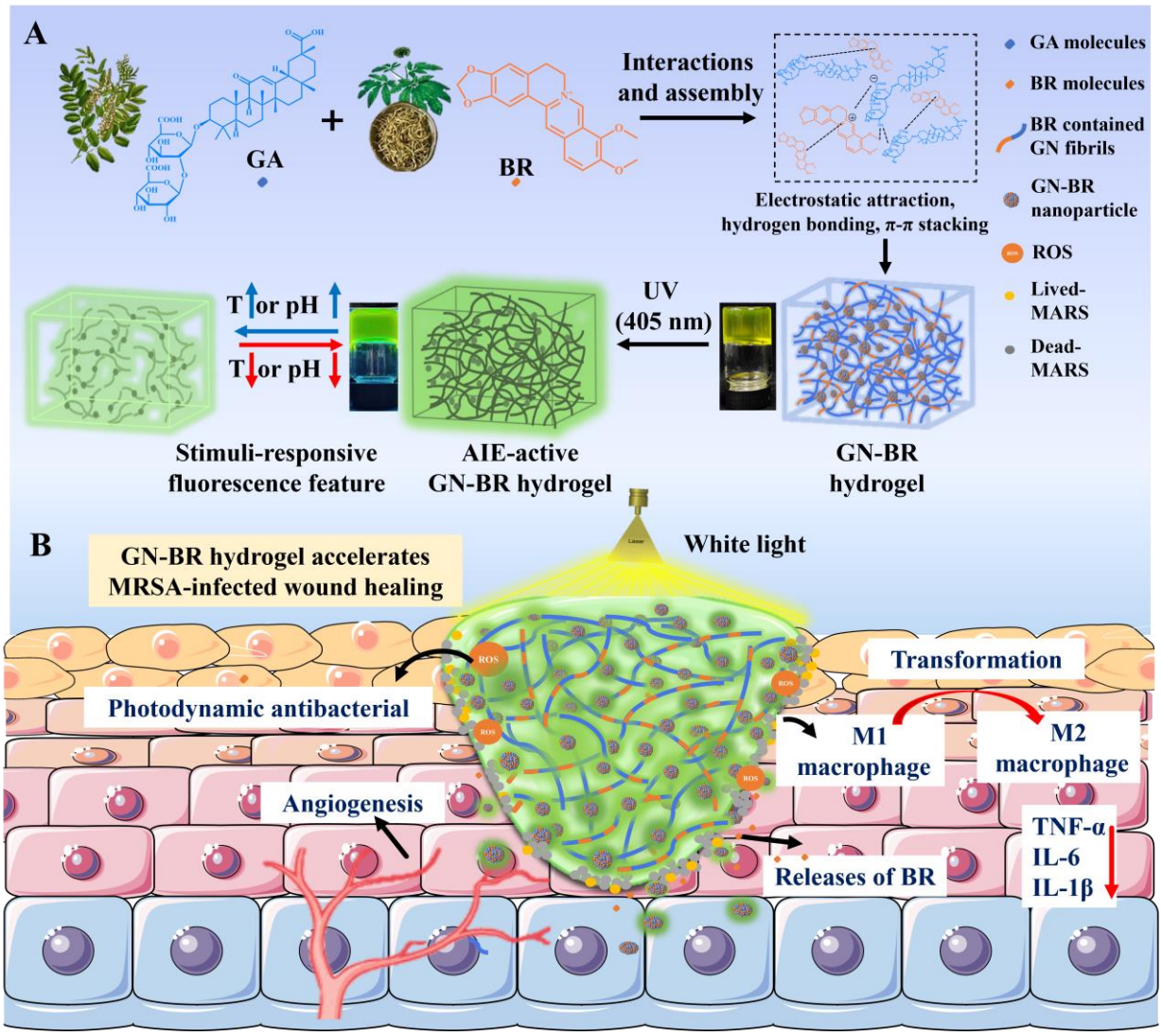

945

946 **Scheme 1.** Illustration of GN-BR AIE-active Hydrogel for MRSA-Infected wound repair. (A)
947 Formation, structural property, and stimuli-responsive fluorescence feature of GN-BR AIE-active
948 hydrogels, and (B) the roles of GN-BR hydrogels in accelerating MRSA-infected wound healing
949 through efficient antibacterial (especially photodynamic antibacterial ability) and anti-inflammatory
950 effects, promoting macrophage phenotype transformation from M1 to M2, and accelerating
951 angiogenesis.

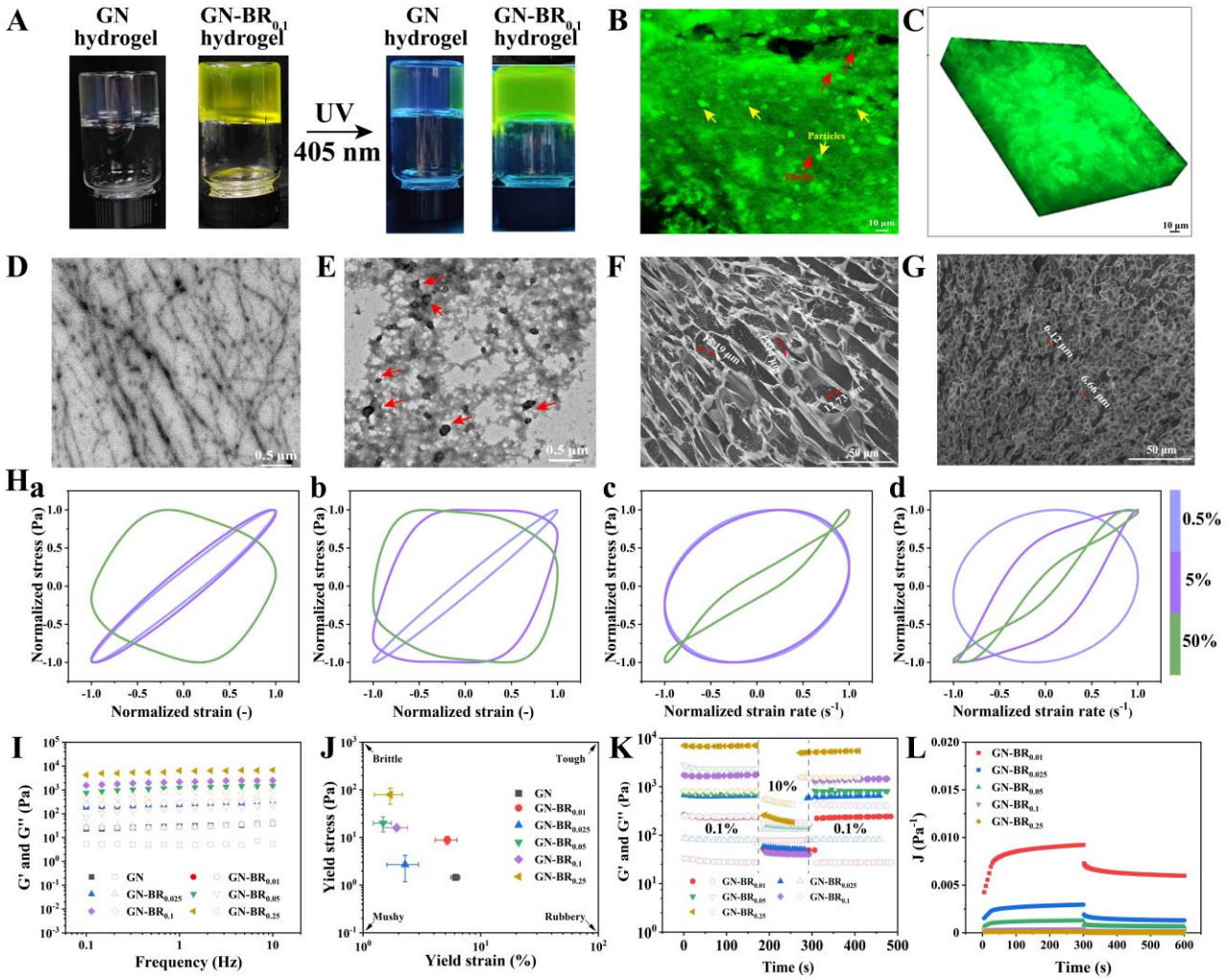

Figure 1. Characterization of GN-BR AIE-active hydrogels. (A) Photographs of 1% GN hydrogel and GN-BR hydrogels with 1% GN and 0.1% BR (GN-BR$_{0.1}$) before (left) and after (right) irradiation by UV light (405 nm). (B) 2D and (C) 3D CLSM images of GN-BR$_{0.1}$ hydrogel under irradiation with excitation at 405 nm; yellow and red arrows represent the assembled GN-BR nanoparticles and the BR-attached GN, respectively. TEM images of (D) GN and (E) GN-BR$_{0.1}$ hydrogels; red arrows mean the GN-BR particles. Cryo-SEM images of (F) GN and (G) GN-BR$_{0.05}$ hydrogels. (Ha and b) Elastic and (Hc and d) viscous normalized Lissajous-Bowditch plots of (a and c) 1% GN and (b and d) GN-BR$_{0.1}$ hydrogels at 0.5, 5, and 50% strain. (I) Frequency sweep, (J) yield strain-stress texture maps, (K) thixotropic curves under low strain (0.1%) and high strain (10%), and (L) creep compliance (J_m) curves of GN-BR hydrogels with 1% GN and different BR concentrations (0, 0.01, 0.025, 0.05, 0.1, and 0.25%). G′ and G″ are shown as filled and open symbols, respectively.

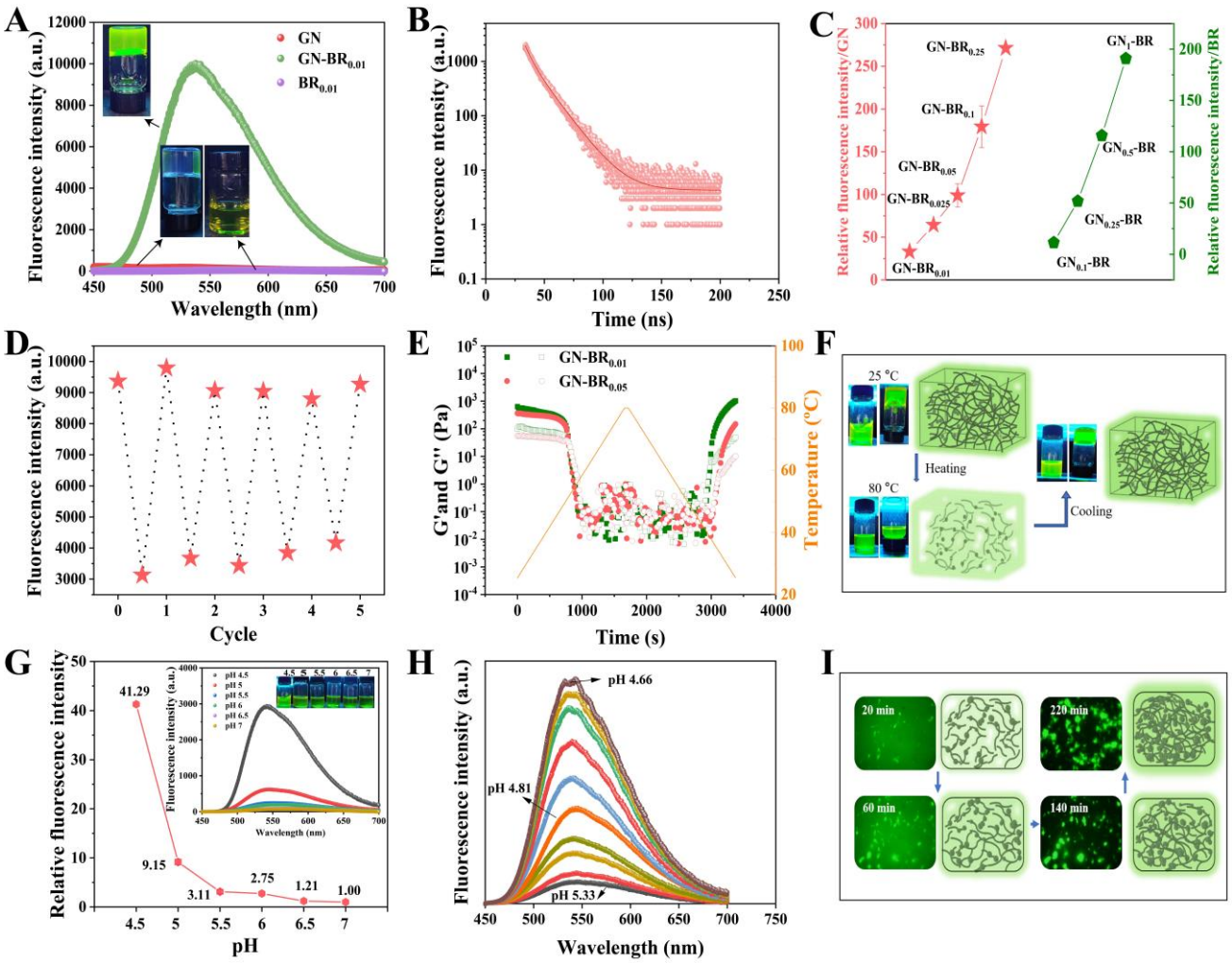

Figure 2. Fluorescence properties of GN-BR AIE-active hydrogels. (A) Fluorescence emission spectra and the corresponding appearance photographs (inset images) of 0.01% BR solution ($BR_{0.01}$), 1% GN hydrogel (GN), and GN-BR hydrogel with 1% GN and 0.01% BR ($GN\text{-}BR_{0.01}$). (B) Time-resolved emission spectra of $GN\text{-}BR_{0.01}$ hydrogel. (C) The relative fluorescence intensity of various GN-BR samples to pure 1% GN hydrogel and 0.1% BR solution. (D) Fluorescence intensity changes at 545.4 nm of $GN\text{-}BR_{0.01}$ hydrogel during heating-cooling cycles for five times from low (25 °C) to high temperature (80 °C) followed by return to 25 °C. (E) Temperature sweep curves of GN-BR hydrogels with 1% GN and different BR concentrations (0.01 and 0.05%, i.e., $GN\text{-}BR_{0.01}$ and $GN\text{-}BR_{0.05}$); G′ and G″ are shown as filled and open symbols, respectively. (F) Photographs and structural schematic diagrams of $GN\text{-}BR_{0.01}$ hydrogel under UV light irradiation (405 nm) after heating from 25 to 80 °C and then returning to 25 °C. (G) The relative fluorescence intensity of GN-

977 $BR_{0.05}$ hydrogels at different pH as compared to that at pH 7; inset images are fluorescence emission
978 spectra and the corresponding fluorescent hydrogel appearances at different pH. (H) Fluorescence
979 emission spectra of GN-$BR_{0.05}$ hydrogel after addition of an acidifying agent (i.e. glucono-delta-
980 lactone) for gradually reducing pH (from 5.33 to 4.66) at different times (10, 20, 60, 90, 120, 140,
981 160, 220, 240, and 260 min), and (I) the corresponding fluorescence images and structural schematic
982 diagrams at different times (20, 60, 140, and 220 min).
983

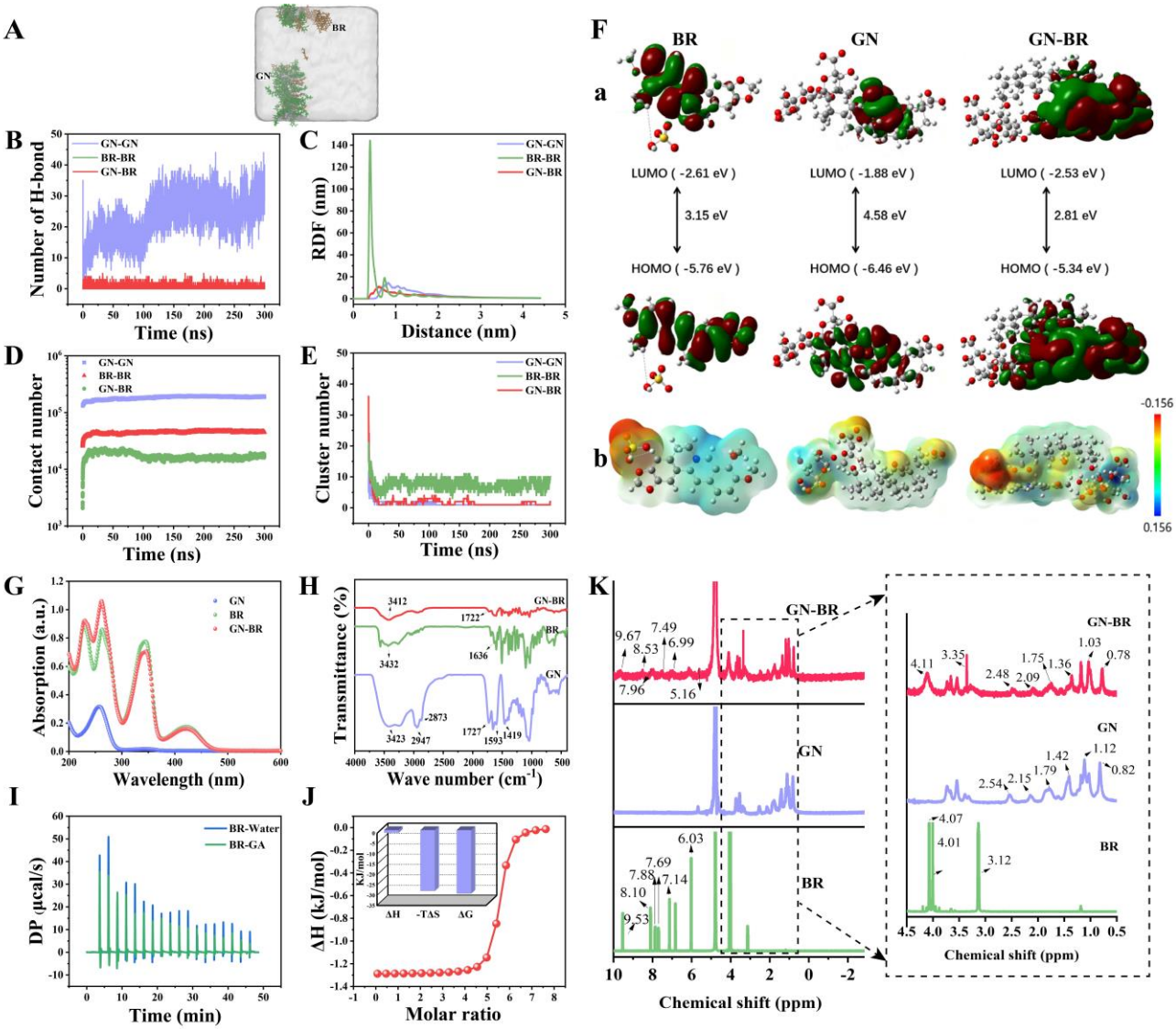

Figure 3. AIE-active and co-assembly mechanism of GN-BR hydrogels. Molecular dynamics (MD) simulations of randomly distributed GN and BR self-assembly in water. (A) The simulation snapshot at the end of the simulation. (B) The hydrogen bond number, (C) radial distribution function (RDF), (D) contact number, and (E) cluster number of BR-BR, GN-GN, or BR-GN pairs in the system. (Fa) Molecular orbital amplitude plots of the highest and the lowest unoccupied orbit (HOMO and LUMO) energy gap of BR, GN, and GN-BR systems. (Fb) The Electrostatic Potential Maps of the three systems. (G) UV-vis, (H) FTIR, and (K) ^{1}H-NMR spectra of GN hydrogel (GN), BR solution (BR), and GN-BR hydrogel. (I) Change in heat flow over time for injection of BR (1%) into the water and GN solutions (0.05%). (J) Representative heat flow change in molar enthalpy (ΔH) for each titration of BR into GN and the calculated thermodynamic parameters after deducting the blank

995 groups.

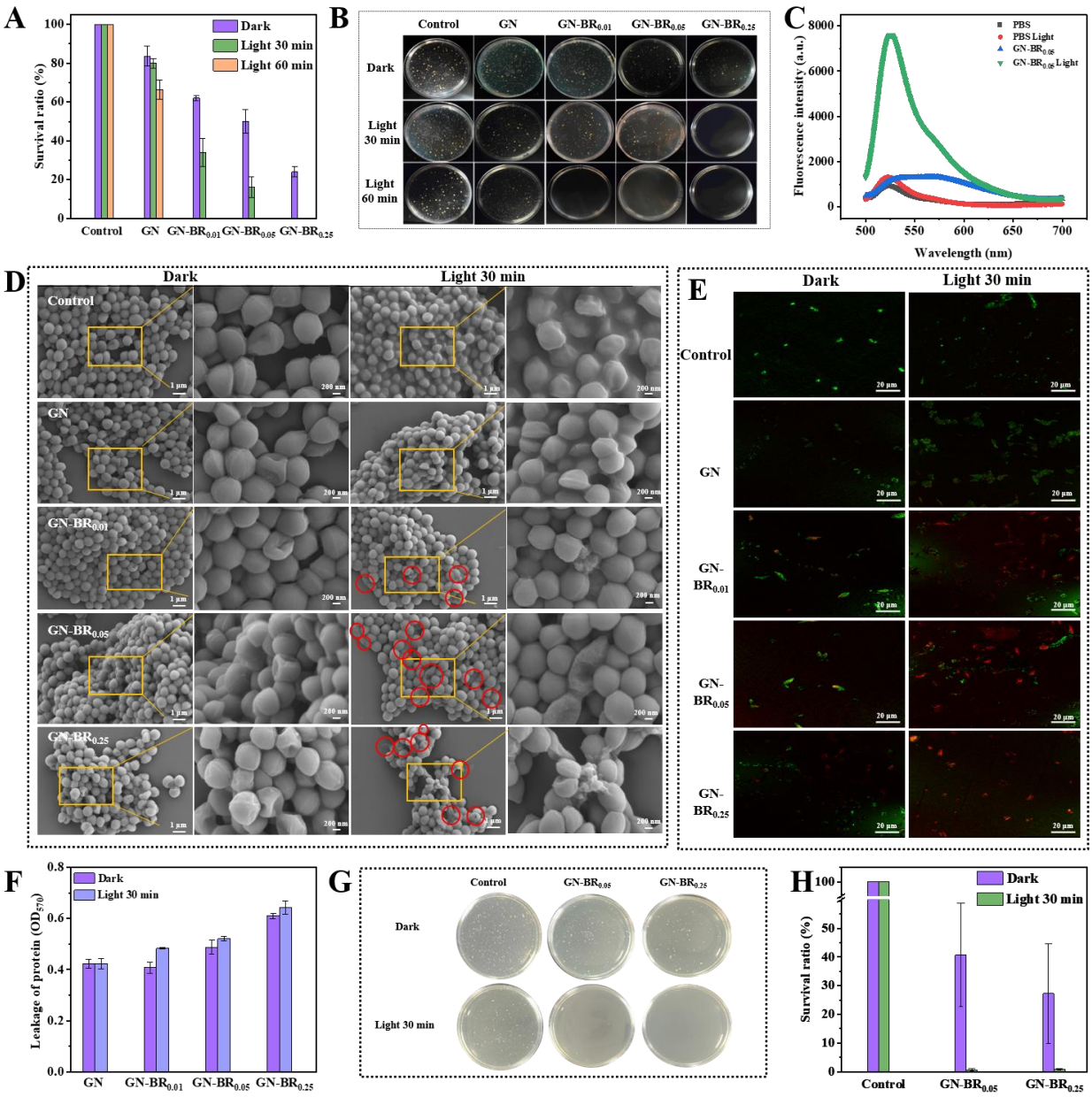

Figure 4. Antibacterial assay of GN-BR AIE-active hydrogels. Survival ratio of (A) *S. aureus* and (H) MRSA after treatments with the sterile PBS solution (pH 7.4) (control), GN hydrogel (GN), and GN-BR hydrogels containing 1% GN and various concentrations of BR (0.01, 0.05, and 0.25%, named as GN-$BR_{0.01}$, GN-$BR_{0.05}$, and GN-$BR_{0.25}$, respectively) with and without white light irradiation (30 and 60 min). (B and G) Photographs of bacterial strains incubated with sterile PBS solution (control) and the hydrogels with and without white light irradiation (30 and 60 min). (D) SEM images and (E) live-dead staining of *S. aureus* after being treated by sterile PBS solution

(control), GN hydrogel (GN), and these GN-BR hydrogels under darkness and light treatment for 30 min. (C) ROS generation efficiency of GN-$BR_{0.05}$ hydrogel under darkness and exposure to visible light for 30 min, and the sterile PBS solutions (pH 7.4) with and without irradiation were used as the control. Higher fluorescence intensity means more efficient ROS production. (F) Leakage of protein from *S. aureus* bacteria after different hydrogel treatments with and without visible light (30 min).

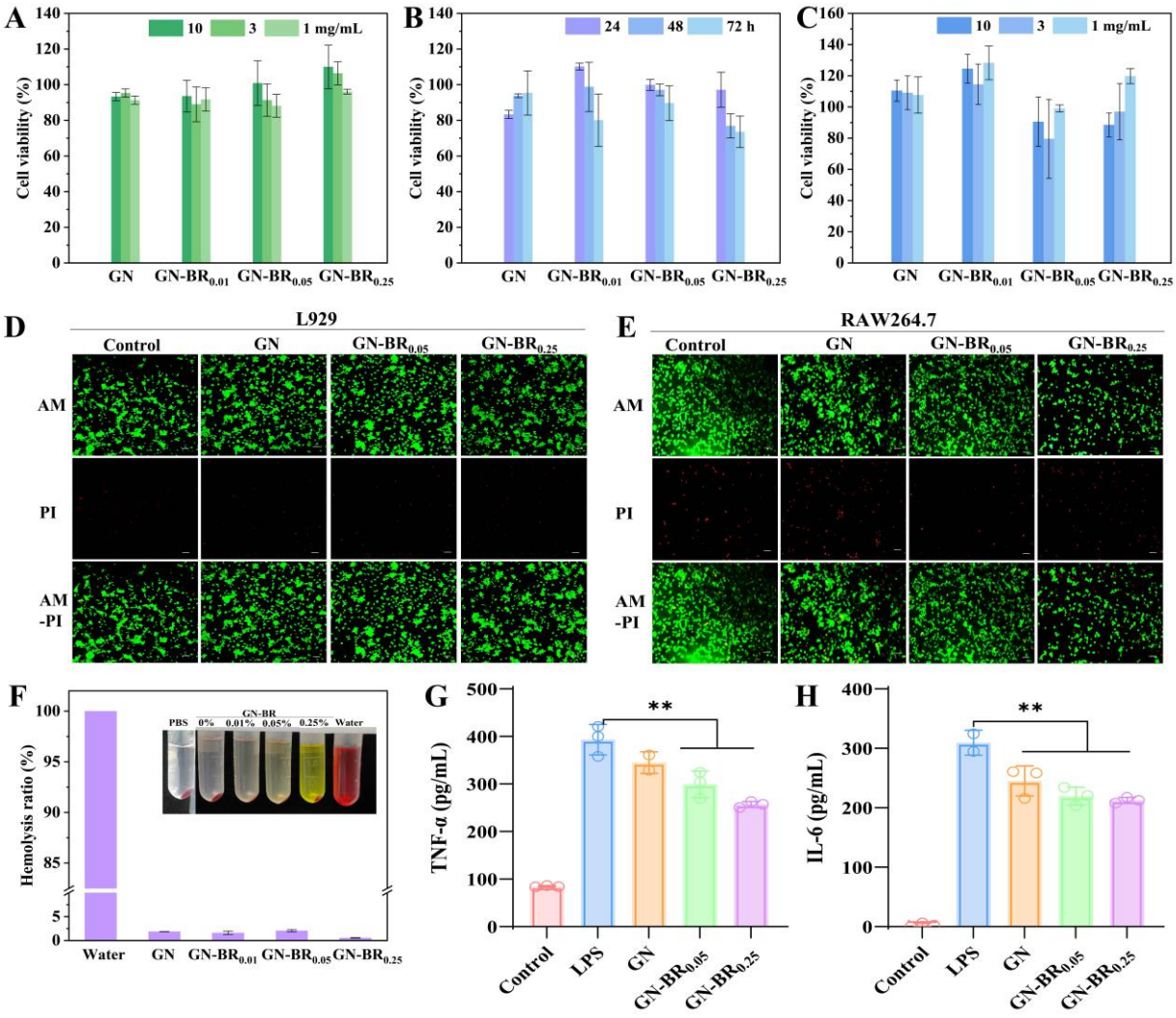

Figure 5. In vitro biocompatibility and anti-inflammation ability of GN-BR AIE-active hydrogels. Viability of (A) L929 and (C) RAW264.7 cells incubated with individual GN-BR hydrogel extracts with different concentrations (1, 3, and 10 mg/mL) for 24 h by MTT assay. (B) Viability of L929 incubated with hydrogel extracts (10 mg/mL) for different times (24, 48, and 72 h). Live-dead fluorescence staining images of (D) L929 and (E) RAW264.7 cells with hydrogel extract liquid (10 mg/mL) for 24 h; live cells were stained by Calcein-AM (AM) with green fluorescence, and dead cells were stained by Propidium Iodide (PI) with red fluorescence. (F) Hemolysis ratio and hemolytic photographs (inset image) after being treated by various GN-BR hydrogels. Intracellular (G) TNF-α and (H) IL-6 levels in LPS-stimulated RAW246.7 cells after being treated with individual GN-BR

hydrogel extracted liquids (10 mg/mL). Values were analyzed by the T-test: *$p < 0.05$, **$p < 0.01$, and ***$p < 0.001$.

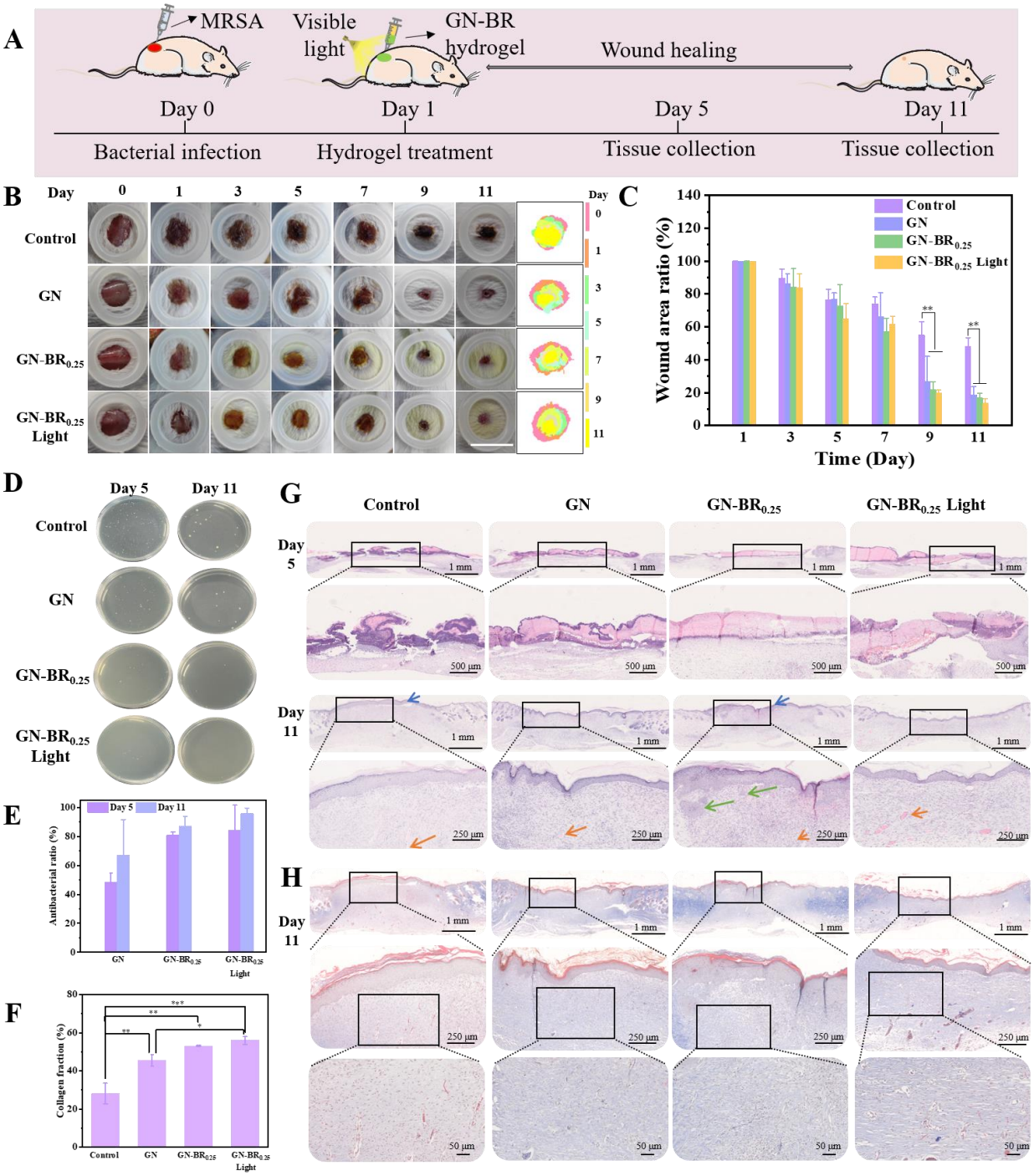

Figure 6. MRSA-infected full-thickness wound healing ability of GN-BR AIE-active hydrogels. (A) Schematic diagram of an MRSA-infected mice model. (B) Representative photographs (Scale bar =1 cm) of wounds and (C) quantified wound closure after treatment with GN hydrogel (GN) and GN-$BR_{0.25}$ hydrogel with and without white visible light irradiation (20 mW/cm^2) for 10 min (i.e., GN-$BR_{0.25}$ and GN-$BR_{0.25}$ Light) at different time points (day 0, 1, 3, 5, 7, 9, and 11). The MRSA-infected mice without treatment were set as control. (D) Photographs of *S. aureus* colony collected from the

infected skin on days 5 and 11, and (E) their survival ratio in different groups as compared to the control group. (G) HE staining images of wound tissues on days 5 and 11. Blue arrows mean the epidermis. Green and orange arrows represent the hair follicle and blood vessels, respectively. (H) Masson's trichrome staining of wound tissues on day 11. (F) Collagen frication of wound tissues on day 11. Values were analyzed by the T-test: $*p < 0.05$, $**p < 0.01$, and $***p < 0.001$.

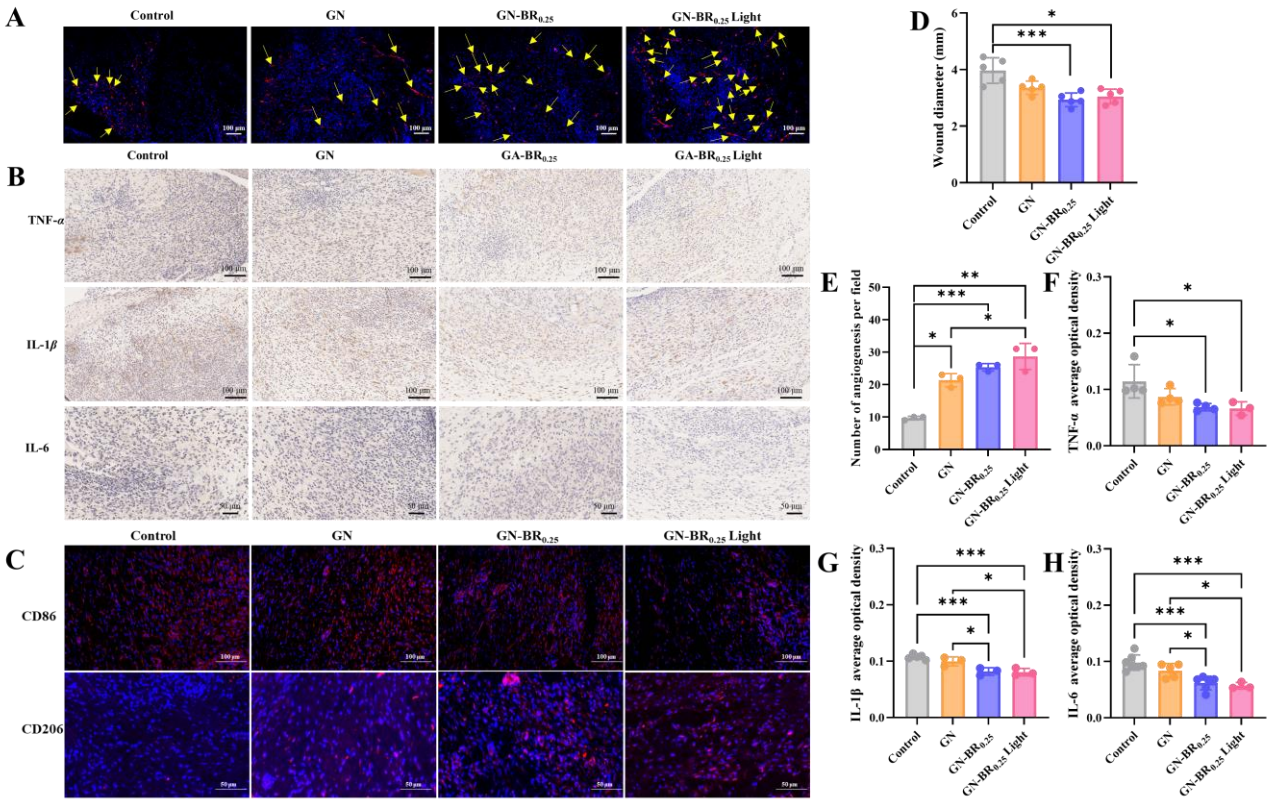

1035

1036 **Figure 7**. Immunohistochemistry analysis of wound tissue after treatments with the hydrogels. (A)
1037 CD31 staining images of wounds (the yellow arrows represent the neovascularization), (D)
1038 quantification of the wound edge, and (E) the calculated amount of angiogenesis per field after
1039 treatment with GN hydrogel (GN) and GN-$BR_{0.25}$ hydrogels with and without white visible light
1040 irradiation (20 mW/cm^2, 10 min) (i.e., GN-$BR_{0.25}$ and GN-$BR_{0.25}$ Light) on day 11. MRSA-infected
1041 mice without any treatment were set as control. (C) Immunofluorescence staining of tissue sections
1042 of wound area for CD86 (M1 marker) and CD206 (M2 marker) at day 11 after injury. (B)
1043 Immunohistochemistry staining images of TNF-α, IL-1β and IL-6, the corresponding average optical
1044 density values (F: TNF-α; G: IL-1β; H: IL-6) of wound tissue on day 5. Values were analyzed by the
1045 T-test: *$p < 0.05$, **$p < 0.01$, and ***$p < 0.001$.